Calhoun: The NPS Institutional Archive

DSpace Repository

Theses and Dissertations | 1. Thesis and Dissertation Collection, all items

2016-09

Microwave-photonic architecture for direction finding of LPI emitters: post-processing for angle of arrival estimation

Ong, Chee Kiong

Monterey, California: Naval Postgraduate School

http://hdl.handle.net/10945/50462

Copyright is reserved by the copyright owner.

Downloaded from NPS Archive: Calhoun

http://www.nps.edu/library

Calhoun is the Naval Postgraduate School's public access digital repository for research materials and institutional publications created by the NPS community. Calhoun is named for Professor of Mathematics Guy K. Calhoun, NPS's first appointed -- and published -- scholarly author.

Dudley Knox Library / Naval Postgraduate School
411 Dyer Road / 1 University Circle
Monterey, California USA 93943

NAVAL POSTGRADUATE SCHOOL

MONTEREY, CALIFORNIA

THESIS

MICROWAVE-PHOTONIC ARCHITECTURE FOR DIRECTION FINDING OF LPI EMITTERS: POST-PROCESSING FOR ANGLE OF ARRIVAL ESTIMATION

by

Chee Kiong Ong

September 2016

Thesis Advisor: Phillip E. Pace
Second Reader: David C. Jenn

Approved for public release. Distribution is unlimited.

THIS PAGE INTENTIONALLY LEFT BLANK

REPORT DOCUMENTATION PAGE			Form Approved OMB No. 0704–0188

Public reporting burden for this collection of information was estimated to average 1 hour per response, including the time for reviewing instruction, searching existing data sources, gathering and maintaining the data needed, and completing and reviewing the collection of information. Send comments regarding this burden estimate or any other aspect of this collection of information, including suggestions for reducing this burden, to Washington headquarters Services, Directorate for Information Operations and Reports, 1215 Jefferson Davis Highway, Suite 1204, Arlington, VA 22202-4302, and to the Office of Management and Budget, Paperwork Reduction Project (0704-0188) Washington, DC 20503.

1. AGENCY USE ONLY *(Leave blank)*	2. REPORT DATE September 2016	3. REPORT TYPE AND DATES COVERED Master's thesis

4. TITLE AND SUBTITLE
MICROWAVE-PHOTONIC ARCHITECTURE FOR DIRECTION FINDING OF LPI EMITTERS: POST-PROCESSING FOR ANGLE OF ARRIVAL ESTIMATION

5. FUNDING NUMBERS

6. AUTHOR(S) Chee Kiong Ong

7. PERFORMING ORGANIZATION NAME(S) AND ADDRESS(ES)
Center for Joint Services Electronic Warfare, Naval Postgraduate School
Monterey, CA 93943-5000

8. PERFORMING ORGANIZATION REPORT NUMBER

9. SPONSORING /MONITORING AGENCY NAME(S) AND ADDRESS(ES)
Consortium for Robotics and Unmanned Systems Education and Research (CRUSER)

10. SPONSORING / MONITORING AGENCY REPORT NUMBER

11. SUPPLEMENTARY NOTES The views expressed in this thesis were those of the author and do not reflect the official policy or position of the Department of Defense or the U.S. Government. IRB Protocol number ____N/A____.

12a. DISTRIBUTION / AVAILABILITY STATEMENT
Approved for public release. Distribution is unlimited.

12b. DISTRIBUTION CODE

13. ABSTRACT (maximum 200 words)

Direction finding (DF) systems are fundamental electronic support measures for electronic warfare. A number of DF techniques have been developed over the years; however, these systems are limited in bandwidth and resolution and suffer from a complex design for frequency down-conversion. An innovative design of a microwave-photonic direction finding technique for the detection and direction finding of low probability of intercept (LPI) signals is investigated in this thesis. Key advantages of this design include a small baseline, wide bandwidth, high resolution, and minimal space, weight, and power requirement. A unique phase encoding method is used to resolve the ambiguities over the entire field-of-view with high accuracy. Experimental tests using frequency-modulated continuous wave (FMCW) and continuous wave (CW) P4 modulated signals were conducted in an anechoic chamber to verify the system design. Test results showed that the microwave-photonic DF system has a sensitivity of –62.96 dBm and is capable of measuring the angle-of-arrival (AOA) of the LPI signals with <1° resolution over a 180° field-of-view. For an FMCW signal, it was demonstrated that the system is capable of estimating the AOA with a root-mean-square (RMS) error of 0.29° at <1° resolution. For a P4 coded signal, the RMS error in estimating the AOA is 0.32° at 1° resolution.

14. SUBJECT TERMS
Direction finding, DF, LPI signals, minimum Euclidean distance detection, photonics, Mach Zehnder modulator, MZM, angle of arrival, AOA

15. NUMBER OF PAGES
91

16. PRICE CODE

17. SECURITY CLASSIFICATION OF REPORT	18. SECURITY CLASSIFICATION OF THIS PAGE	19. SECURITY CLASSIFICATION OF ABSTRACT	20. LIMITATION OF ABSTRACT
Unclassified	Unclassified	Unclassified	UU

NSN 7540–01-280-5500

Standard Form 298 (Rev. 2–89)
Prescribed by ANSI Std. 239–18

THIS PAGE INTENTIONALLY LEFT BLANK

Approved for public release. Distribution is unlimited.

MICROWAVE-PHOTONIC ARCHITECTURE FOR DIRECTION FINDING OF LPI EMITTERS: POST-PROCESSING FOR ANGLE OF ARRIVAL ESTIMATION

Chee Kiong Ong
Civilian, Defence Science and Technology Agency (Singapore)
B.Eng. National University of Singapore, 2005

Submitted in partial fulfillment of the
requirements for the degree of

MASTER OF SCIENCE IN ELECTRICAL ENGINEERING
from the

NAVAL POSTGRADUATE SCHOOL
September 2016

Approved by: Phillip E. Pace
Thesis Advisor

David C. Jenn
Second Reader

R. Clark Robertson
Chair, Department of Electrical and Computer Engineering

THIS PAGE INTENTIONALLY LEFT BLANK

ABSTRACT

Direction finding (DF) systems are fundamental electronic support measures for electronic warfare. A number of DF techniques have been developed over the years; however, these systems are limited in bandwidth and resolution and suffer from a complex design for frequency down-conversion. An innovative design of a microwave-photonic direction finding technique for the detection and direction finding of low probability of intercept (LPI) signals is investigated in this thesis. Key advantages of this design include a small baseline, wide bandwidth, high resolution, and minimal space, weight, and power requirement. A unique phase encoding method is used to resolve the ambiguities over the entire field-of-view with high accuracy. Experimental tests using frequency-modulated continuous wave (FMCW) and continuous wave (CW) P4 modulated signals were conducted in an anechoic chamber to verify the system design. Test results showed that the microwave-photonic DF system has a sensitivity of –62.96 dBm and is capable of measuring the angle-of-arrival (AOA) of the LPI signals with <1° resolution over a 180° field-of-view. For an FMCW signal, it was demonstrated that the system is capable of estimating the AOA with a root-mean-square (RMS) error of 0.29° at <1° resolution. For a P4 coded signal, the RMS error in estimating the AOA is 0.32° at 1° resolution.

THIS PAGE INTENTIONALLY LEFT BLANK

TABLE OF CONTENTS

I. INTRODUCTION....1
A. PHOTONIC SYSTEM FOR LOW PROBABILITY OF INTERCEPT SIGNALS DETECTION AND DIRECTION FINDING....1
1. Direction Finding....1
2. LPI Signals....3
B. PRINCIPAL CONTRIBUTIONS....5
C. THESIS OUTLINE....6

II. PHOTONIC DF SIGNAL PROCESSING SYSTEM....7
A. PREVIOUS SYSTEM DESIGN....7
B. SYSTEM MODIFICATIONS....9
1. Deterministic Signal Acquisition with Compact-RIO....9
2. Minimum-Euclidean Distance Detector for AOA Estimation....11

III. SYSTEM DESIGN AND TEST SETUP....13
A. NEW SYSTEM ARCHITECTURE....13
B. COMPONENTS USED IN DF SYSTEM DESIGN....14
1. Mach-Zehnder Modulator....14
2. Photo Detector....17
3. Envelope Detector....19
C. SYSTEM CALIBRATION....19
D. SOFTWARE ARCHITECTURE DESIGN....24
E. TEST EQUIPMENT....27
1. Test Setup....28
2. Test Procedure and Data Collection....30

IV. SYSTEM SIMULATION....33
A. SIMULATION OF MZM....33
B. FULL SYSTEM SIMULATION....40

V. TEST RESULTS....43
A. P4 TEST RESULTS....44
B. FMCW TEST RESULTS....49
C. ANALYSIS OF OUTLIERS DATA....53
1. P4 Outlier Data Collected on July 6, 2016....53

2. P4 Outlier Data Collected on July 13, 2016 56
3. FMCW Outlier Data Collected on July 6, 2016 57
4. FMCW Outlier Data Collected on July 13, 2016 59

VI. CONCLUDING REMARKS AND FUTURE CONSIDERATIONS 61

APPENDIX. MATLAB CODE FOR SYSTEM SIMULATION 65

LIST OF REFERENCES 69

INITIAL DISTRIBUTION LIST 71

LIST OF FIGURES

Figure 1. Block Diagram of Previous System. Source [14]. 8

Figure 2. cRIO Signal Acquisition Architecture 10

Figure 3. New System Architecture 13

Figure 4. Photonic DF System Design (Back-end) 14

Figure 5. Schematic of the MZM 15

Figure 6. Actual $LiNbO_3$ MZM used in DF System. Source [23]....15

Figure 7. MZM Transfer Function 17

Figure 8. New Focus 1014 PD. Source: [24]. 18

Figure 9. Frequency Response of New Focus 1014 PD. Source: [24]. 19

Figure 10. MZM Modules with Inputs (blue RF cables) from the RF Front end 20

Figure 11. PD and Envelope Detector Modules with Optical Inputs from MZMs 20

Figure 12. Calibration Setup for Front-end Antenna Sub-system....21

Figure 13. Matched Response for MZM#1: Ch1–Ch3 Are Signals from Reference Antenna, Ch4 Is Signal from Antenna1 22

Figure 14. Matched Response for MZM#2: Ch1–Ch3 Are Signals from Reference Antenna, Ch4 Is Signal from Antenna2....23

Figure 15. Matched Response for MZM#3: Ch1–Ch3 Are Signals from Reference Antenna, Ch4 Is Signal from Antenna3....23

Figure 16. Variable Connectors to Adjust Optical Polarization at MZM Input....24

Figure 17. FPGA Code for DMA Transfer to cRIO Controller 25

Figure 18. cRIO Controller Code to Read Sampled Data and Write to Processing Computer 26

Figure 19. Processing Computer Code to Read Data from cRIO Controller via TCP Protocol....26

Figure 20. Linear FMCW Signal with 100-kHz Modulation Bandwidth and a 100 ms Modulation Period....27

Figure 21. Phase Change in P4 Waveform Captured by RT2044 Oscilloscope 28
Figure 22. Photonic DF System in Anechoic Chamber 29
Figure 23. Transmission Antenna in Anechoic Chamber 29
Figure 24. Raw FMCW Data Collected on July 6, 2016 31
Figure 25. Simulated MZM Response for Saw-tooth Function 34
Figure 26. Actual MZM Response for Saw-tooth Function.....35
Figure 27. Simulated MZM Response for Sinewave Function 35
Figure 28. Actual MZM Response for Sinewave Function.....36
Figure 29. MZM Output for Linear FMCW Input with 0° Phase Shift 37
Figure 30. MZM Output for Linear FMCW Input with 45° Phase Shift 37
Figure 31. MZM Output for Linear FMCW Input with 90° Phase Shift 38
Figure 32. MZM Output for P4 Input with 0° Phase Shift.....38
Figure 33. MZM Output for P4 Input with 45° Phase Shift.....39
Figure 34. MZM Output for P4 Input with 90° Phase Shift.....39
Figure 35. Simulated Response of DF System with Linear FMCW Signal.....40
Figure 36. Phase Representation of P4 Signal Used for Experimental Tests.....44
Figure 37. P4 Data after Post-processing and Normalization (July 6, 2016).....45
Figure 38. P4 AOA Estimation for Angle Sweep from –90° to +90° (July 6, 2016) 46
Figure 39. P4 Signal Error Plot (July 6, 2016).....46
Figure 40. P4 Data after Post-processing and Normalization (July 13, 2016).....47
Figure 41. P4 AOA Estimation for Angle Sweep from –90 to +90 (July 13, 2016) 48
Figure 42. P4 Signal Error Plot (July 13, 2016).....48
Figure 43. FMCW Data after Post-processing and Normalization (July 6, 2016).....49

Figure 44. FMCW AOA Estimation for Angle Sweep from –90° to +90° (July 6, 2016) 50

Figure 45. FMCW Signal Error Plot (July 6, 2016) 50

Figure 46. FMCW Data after Post-processing and Normalization (July 13, 2016) 51

Figure 47. FMCW AOA Estimation for Angle Sweep from –90 to +90 (July 13, 2016) 52

Figure 48. FMCW Signal Error Plot (July13, 2016) 52

Figure 49. Outlier Data Extracted from P4 Signal (July 6, 2016) 54

Figure 50. P4 Outlier Data #17856 to #17869 (July 6, 2016) 55

Figure 51. Raw Input Data that Correlates with the Outliers' Sample Numbers (P4 Signal) 55

Figure 52. Zoom-in View Showing P4 Outliers 56

Figure 53. P4 Outlier Data #2456 to #2491 (July 13, 2016) 57

Figure 54. FMCW Outlier Data #18193 to #18195 (July 6, 2016) 58

Figure 55. FMCW Outlier Data #3708 to #3774 (July 13, 2016) 59

Figure 56. Test Setup for P4 Signal Identification 62

Figure 57. Envelope of Output of MZM for P4 signal 63

THIS PAGE INTENTIONALLY LEFT BLANK

LIST OF TABLES

Table 1. Partial Mapping of Basis Vectors $\tilde{s}_i$ 11

Table 2. New Focus 1014 PD Specifications. Adapted from [25]..... 18

Table 3. Measured Optical Input and Output Power of MZMs..... 24

Table 4. Result Summary of Tests Conducted..... 53

Table 5. Minimum-Euclidean Distance Calculations for Outliers #17866 and #17869..... 54

Table 6. Minimum-Euclidean Distance Calculations for Outliers #2471 and #2481..... 57

Table 7. Minimum-Euclidean Distance Calculations for Outliers #18193 and #18195..... 58

Table 8. Minimum-Euclidean Distance Calculations for Outliers #3708 and #3774..... 60

THIS PAGE INTENTIONALLY LEFT BLANK

LIST OF ACRONYMS AND ABBREVIATIONS

ADC	analog-to-digital converter
AOA	angle-of-arrival
CPP	cycle per phase
cRIO	Compact-RIO
CW	continuous wave
DC	direct current
DE-MZM	dual-electrode Mach-Zehnder modulator
DF	direction finding
DFB	distributed feedback
FMCW	frequency-modulated continuous wave
FPGA	field-programmable gated array
InGaAs	indium gallium arsenide
$LiNbO_3$	lithium niobate
LNA	low noise amplifier
LPI	low probability of intercept
MLP	multi-layered perceptron
MZM	Mach-Zehnder Modulator
PCB	printed circuit board
PD	photodetector
RF	radio frequency
RMS	root-mean-square

THIS PAGE INTENTIONALLY LEFT BLANK

ACKNOWLEDGMENTS

The successful completion of this thesis would not have been possible without the guidance, support, and encouragement from some of the most wonderful people that I have come to know and respect throughout the course of this work.

First, I would like to express my heartfelt gratitude toward my thesis advisor, Professor Phillip E. Pace. Your vision and passion for the project has motivated me to pursue this project more fully than I originally planned. Thank you for the invaluable technical insights that were pivotal in helping me to overcome the challenges faced during the system development. I consider it an honor and privilege to have learned from the best.

I would also like to thank the three most awesome and inspiring lab directors, Dr. James Calusdian, Paul Buczynski, and Bob Broadston. Your unreserved sharing of knowledge and technical advice has been a beacon of hope during some of the most trying phases of the project. I would never have come this far without you.

Many of the lab results would not have been possible without the equipment and technical support from Rohde and Schwarz. I would like to thank Berry Carone and P. B. Balasubramanium for their generosity and support.

Special mention goes out to my lab partner, Eric Tan Chew Kung. Eric, I will always remember the late nights we endured to get the system working. Sometimes, when the tasks seemed insurmountable, you were one of the greatest sources of encouragement and help. Thank you for the friendship.

To my beloved wife, Yi Hsien, and my two wonderful sons, Nathan and Ethan. I want you to know that I love you all very much, and I know that there were so many occasions that I have fallen short of my duty as a husband and father. Thank you for your unconditional love and support. It has meant the world to me.

This project was supported by Naval Postgraduate School (NPS) Consortium for Robotics and Unmanned Systems Education and Research (CRUSER).

THIS PAGE INTENTIONALLY LEFT BLANK

I. INTRODUCTION

A. PHOTONIC SYSTEM FOR LOW PROBABILITY OF INTERCEPT SIGNALS DETECTION AND DIRECTION FINDING

Advancements in digital signal processing and solid-state technologies have led to the proliferation of low probability of intercept (LPI) radars. This class of radar transmits special waveform types with the objective of preventing detection or tracking by non-cooperative intercept receivers [1]. When guided missiles or anti-radiation missiles are equipped with LPI radars, they become a formidable threat to ground-based, airborne, or shipboard radars as the missiles can home in on their target without themselves being detected. To this end, much attention has been placed on developing new and effective techniques to detect threats emitting LPI signals and to estimate their angle-of-arrival (AOA).

LPI signals have several characteristics that help them to avoid detection in the electromagnetic domain [2]. Conventional radar transmits a short pulse with very high peak power, making it highly visible to non-cooperative radars. By contrast, LPI radar signals are modulated continuous wave (CW) signals with the same amount of power distributed over a much longer duration. Consequently, there is no surge in its transmit power to make it easily detectable. The transmission of LPI signals with sophisticated modulation and high processing gain enable a good detection range and low signature in the electromagnetic domain.

1. Direction Finding

Techniques of direction finding (DF) and the characteristics of LPI signals used in LPI radar design are presented in the following section with the intent to provide a more complete understanding of the advantages of using the microwave-photonic approach for direction finding of LPI signals.

Techniques for DF of incident electromagnetic waves can be broadly classified into four types: amplitude, interferometry (phase) DF, Doppler and time-difference-of-

arrival measurement [3]. The choice of which technique to employ often depends on the accuracy requirement, complexity of system design, and cost of system development.

a. Amplitude

Among the different DF techniques, angle estimation based on amplitude measurement typically has the poorest performance. Nevertheless, this technique is still favored at times for its ease of implementation. Amplitude-based DF can be accomplished using a single direction antenna, the Watson-Watt technique [4] or using multiple directional antennas. Most radar warning receivers that employ amplitude DF use the multiple directional antennas technique as it provides wide frequency response with relatively stable signal gain estimation.

b. Interferometry DF

Interferometry DF is a highly accurate means of estimating the AOA of an incident wave by measuring the phase differences of the wave at the receiving antennas. A root-mean-square (RMS) error of 1° is achievable with this DF technique, but the actual performance of interferometry DF is highly dependent on the phase matching between the receiving antennas as well as the number of receiving antennas. A higher operating frequency has a more stringent phase matching requirement, while increasing the number of receiving antennas improves the AOA estimation accuracy. Compared to the amplitude DF systems, interferometry DF systems are generally more complex and costly to implement.

c. Doppler

The AOA of an electromagnetic wave can also be estimated by using a pair of rotating antennas to measure the absolute Doppler received. The estimated AOA corresponds to the zero Doppler rotation angles. There are two challenges involved in this method; the first is the mechanical difficulties of rotating one antenna in a constant fashion around another. Using a larger number of antennas and switching quickly between these antennas to create a rotation effect can overcome this problem. The second challenge has to do with accuracy determination of the transmit frequency in order to

compute the absolute Doppler. In most situations, the receive frequency cannot be known with high precision. For this reason, the differential Doppler DF technique was developed [5]. In general, Doppler DF achieves better accuracy compared to amplitude DF, but its implementation is significantly more complex.

d. Time Difference of Arrival

The last technique uses time-difference-of-arrival at two receivers to determine the AOA of a signal [6]. This technique requires very precise synchronization between the receivers. With a Global Positioning System, synchronization on the order of several nanoseconds can be achieved, making this DF technique extremely accurate for receiver antennas with a large baseline. Due to the requirement for a large antenna baseline, such a technique is not practical for single-platform DF.

2. LPI Signals

There are numerous types of signals suitable for deployment in LPI radars. Most of them fall under one of the following categories.

a. Frequency-Modulated Continuous Wave Signals

Frequency-modulated continuous wave signals (FMCW) are favored in radar design due to their implementation simplicity and the high range resolution that can be achieved with such signals [7]. Sinusoidal and linearly modulated FMCW are two of the most commonly used signals as they can be easily generated with a simple hardware architecture. Furthermore, these wideband signals cannot be handled easily by non-cooperative radars equipped with conventional super-heterodyne receivers.

b. Phase-Shift Keying Signals

The phase-shift keying signal, also known as polyphase or polytime signal, is another variant of LPI signal that has very wide bandwidth and low side-lobe levels as compared to FMCW signals [8], [9]. This characteristic makes it extremely difficult to detect and identify in an operational environment. Some examples of phase-shift keying signals include Barker polyphase sequence, Frank code, P1, P2, P3, and P4. These

waveforms are highly compatible with digital generation devices, making them an attractive candidate for both research and actual implementation.

c. Frequency-Shift Keying Signals

Another class of LPI signal is a frequency-shift keying signal that is able to provide very high processing gain by transmitting a frequency-hopping signal over a very wide bandwidth [10]. Since the frequency hopping sequence is unknown to non-cooperative intercept radars, identification of the waveform is extremely difficult; however, unlike FMCW and phase-shift keying signals, each hop of the frequency-shift keying signal has a relatively high transmit power, making them more susceptible to detection by intercept receivers.

d. Noise Signals

The last class of LPI signals is known as random or pseudorandom noise signals. Early works using noise signals for radars were reported by the Institute of Radio Electronics [11], [12]. Subsequent research demonstrated the concept of using random noise signals for LPI radar [13]. Random noise signals are typically ultra-wideband, with extremely high processing gain and high immunity against interference.

It is evident that most LPI signals are wideband signals with relatively low instantaneous power. To detect such signals, conventional DF receivers need to scan a very wide microwave spectrum, and the down-conversion RF chain further reduces the signal-to-noise ratio. Both of these factors have the cumulative effect of reducing the probability of LPI signal detection.

Conventional DF system design based on super-heterodyne receivers has a relatively narrow real-time bandwidth that is not ideal for LPI signal detection. The complex hardware architecture of these systems often results in high space, weight, and power demands. By contrast, the photonic DF system is a novel approach that utilizes the Mach Zehnder modulator as a phase detector with an extremely large real-time bandwidth capable of handling wideband LPI signals. It has the added advantage of being able to perform phase difference measurement in the RF spectrum without the need for

frequency down-conversion. Consequently, this photonic DF system avoids the design complexities associated with super-heterodyne receivers, making it a highly compact DF system that is suitable for deployment on small platforms.

Research into microwave-photonic DF systems is divided into two parts: (1) the front-end microwave photonics circuit and (2) the photonic phase detection and post-processing for AOA estimation. The focus of this thesis is on the latter, and its principal contributions are presented in the following section.

B. PRINCIPAL CONTRIBUTIONS

In this thesis, early works on the use of the dual-electrode Mach-Zehnder modulators (DE-MZM) for direction finding are analyzed [14]. Predecessor system design and architecture were also investigated [15]. Various design improvements were made to the system front-end and back-end to improve the system performance and capabilities [16].

The original design utilized back-end digital processing to provide dynamic control of the front-end attenuators and T-biases. These control lines were replaced with standalone voltage dividers at the front-end. Empirical observations have shown that dynamic tuning of front-end parameters is not necessary for the system as its performance remains stable once calibrated. This redesign simplifies the overall system complexity and reduces the processing burden on the back-end controller.

To improve the system calibration efficiency and to simplify system maintenance efforts, the previous system was modularized into four sub-systems consisting of the front-end signal equalizing and amplification module, the signal conditioning module, the optical MZM module, and the photo detection and digitalizing module. This modularized design allows highly targeted testing and calibration of sub-functionalities such as the RF-to-optical conversion process in the MZM without having to cope with the system uncertainties from other sub-functions.

The first major contribution of this work is the demonstration of the system's capability to detect and estimate the AOA of LPI signals such as FMCW and P4 waveforms.

The second contribution is the design and implementation of minimum-Euclidean distance detection for estimating the AOA of LPI signals. Experimental testing of the system was carried out in the anechoic chamber, and it was shown that this estimation strategy does not require frequent system calibration or any form of system training and is also capable of providing consistent and accurate results throughout the entire experimental test duration.

The third contribution is the development of a simulation model for the photonic direction finding system. This software is capable of providing a back-of-the-envelope estimation for the expected response of LPI signals such as FMCW waveforms. This simulation model can be extended to assess the system's feasibility in handling other types of signals.

The fourth contribution is the overhaul of the back-end real-time processing software. The new design can deliver deterministic sampling up to 100 kHz when equipped with the proper hard disk data streaming devices. Future designs could leverage this enhancement to detect time-varying pulse waveforms.

C. THESIS OUTLINE

The objective of this thesis is to review the design and capability of an existing system and to incorporate enhancements to that system with the primary objective of performing LPI signal detection and direction finding. The previously existing system is described in Chapter II, which also provides a discussion on major system modifications and improvement. In Chapter III, the new system design is presented along with an overview of the theory of Mach Zehnder operation, which plays a key role in the overall system design. This chapter also touches on the system calibration procedures, upgrades to the existing software architecture, and the system testing and data collection process. The software simulation of the system, which supports the hypothesis that the physical system is capable of detecting LPI signals, is presented in Chapter IV. The physical experimental results and analyses are presented in Chapter V, and the concluding remarks as well as recommendations for future research in this area are provided in Chapter VI.

II. PHOTONIC DF SIGNAL PROCESSING SYSTEM

An overview of the previous system used for the direction finding of a single CW test signal in the anechoic chamber is provided in this chapter and major improvements and modifications to the design are discussed.

A. PREVIOUS SYSTEM DESIGN

A system block diagram of the previous photonic DF system is shown in Figure 1 [14]. By using the concept of a robust symmetrical number system, an antenna array with a small baseline for a DF system can be achieved [17]. Experimental tests were conducted on the system in the anechoic chamber to characterize the DF performance of the system for a single CW transmitter at 2.4 GHz. The signal was generated using the HP 83711B Synthesized CW Generator with an output power of 1 dBm and amplified by a HP 8348A amplifier to 25 dBm. The transmitted signal was received by an array of four dipole antennas printed on printed circuit boards. These signals were subsequently amplified by low noise amplifiers (LNA) and routed through phase shifters to the DE-MZMs.

A high-power distributed feedback (DFB) laser operating at the 1550 nm wavelength optically drives the MZMs. The optical signal within each MZM modulates the 2.4-GHz CW signals applied at its electrodes. The optical output amplitude of the MZM takes on a value that is proportionate to the phase difference of the radio frequency (RF) signal between its two electrodes. Each of the optical outputs of the MZM is converted back to electrical signal using indium gallium arsenide (InGaAs) photodetectors (PD).

After the PD stage, the amplitudes of the modulated signals were measured to determine the phase differences of the three antenna pairs in the system. This was achieved by first removing any DC in the signals using DC blocking capacitors and then using envelope detectors to filter out the carrier frequencies in the signals. Two subsequent stages of amplification were added to bring the signal level to a suitable range for the analog-to-digital converter (ADC). Sampling of the signals was done using a

compact-RIO (cRIO) real-time controller, and these samples were streamed to a separate computer for further post-processing. A two-layer multilayer perceptron (MLP) neural network was used to estimate the AOA from the raw sampled data. This neural network was trained using data collected from the system in the anechoic chamber.

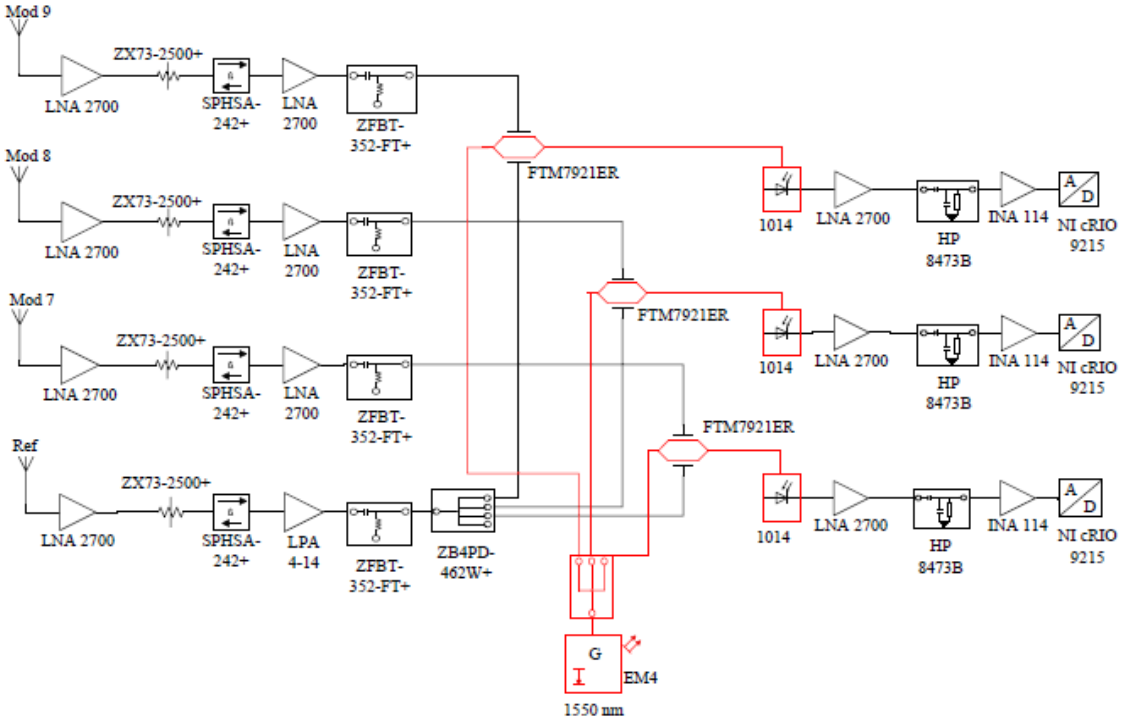

Figure 1. Block Diagram of Previous System. Source [14].

During the preliminary investigation of the system operation, it was found that the phase shifters that were incorporated to introduce a phase shift between the antennas were unnecessary as the inherent spacing between the antenna elements provided the desired phase offset for proper AOA estimation using the MZMs. In addition, voltage dividers replaced the T-bias controlled by the cRIO to ensure that the system operated in the linear region of the MZM. This modification simplifies the system design and operation and reduces the processing burden on the cRIO. From empirical observations, the T-bias value required for linear operation of the MZMs does not drift significantly with time; hence, it does not need to be controlled dynamically using the cRIO. For the

same reason, the digital controls to the front-end attenuators were replaced with voltage dividers to simplify the overall system operation and design.

For the signal-processing segment, it was found that the use of an MLP neural network, although feasible, was too computationally intensive and reduced system responsivity. Furthermore, new training data was constantly required to calibrate the system as the operating conditions changed. To improve the existing design, a minimum-Euclidean distance detector was proposed. This technique does not require the use of training data and frequent system calibration. Experiments conducted in the anechoic chamber have shown that this technique provides good AOA estimation for FMCW and P4 signals. The signal acquisition architecture was also enhanced to perform deterministic acquisition of LPI signals.

B. SYSTEM MODIFICATIONS

The major system modifications and their implications to the overall system performance are described in the following section.

1. Deterministic Signal Acquisition with Compact-RIO

The National Instruments cRIO system was used as the signal acquisition and processing subsystem. The cRIO system consists of a real-time controller operating at 400 MHz with 64 MB of volatile memory and 128 MB of data storage, a Virtex-5 FPGA module to provide high speed deterministic sampling of the DF channels, and a 12-bit, four analog input channels with a sampling rate up to 100 kHz. The real-time capability of the cRIO system was not fully exploited in the previous system design as that design used a single memory-shared variable for data transfer between the cRIO and the signal-processing computer. This meant that in the event that the sampled data was not read from the shared variable before the next sample arrived, the data was overwritten and lost. This form of signal acquisition is non-deterministic and can only be used to sample DC signals. This is not the case for most LPI signals (or pulsed signals), where the waveforms are transmitted only for a brief duration. To cope with such signal behavior, deterministic sampling is required. To achieve this, significant changes to the digital signal acquisition architecture were needed.

The cRIO hardware architecture is shown in Figure 2.

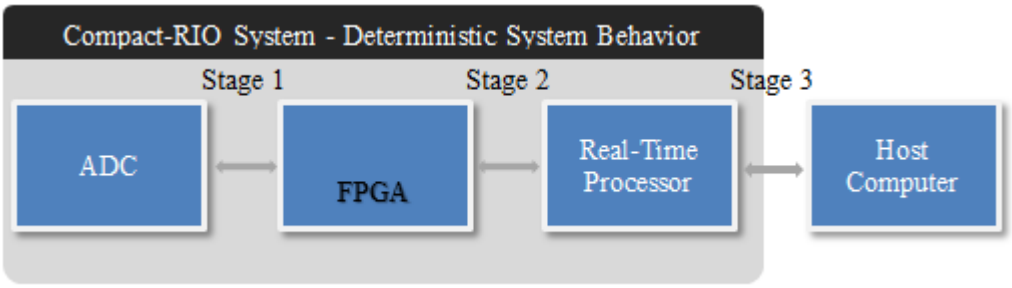

Figure 2. cRIO Signal Acquisition Architecture

The interface between the field-programmable gated array (FPGA) and the ADC, stage 1, was designed to perform sampling at the maximum sampling rate of the ADC in a deterministic fashion. Data processing was reduced as much as possible in this stage to minimize the computational burden on the FPGA, which could affect its real-time behavior. The sampled data then was transferred to the real-time processor via Direct Memory Access in stage 2. This is the most efficient means of data transfer between the real-time processor and FPGA and ensures that the data buffer within the FPGA does not overflow. Finally, to maintain the deterministic behavior of the real-time processor and to prevent buffer overflow in its volatile memory, the sampled data must be transferred to the host computer for further processing and storage. This was done in stage 3 via the network stream protocol that utilizes the transmission control protocol (TCP) to ensure reliable data transfer.

The protocols and software architecture selected were able to maximize the potential of the cRIO system and provide a deterministic sampling rate of 10 kHz for a single channel. The system performance is currently limited by the data stream-to-disk speed of approximately 30 MB/s. With dedicated data streaming hardware running on RAID configurations, the sampling rate of the system can be further enhanced to 100 kHz. This means that the system can potentially capture pulse signals with a minimum pulse duration of 20.0 μs. Sampling rates of 1.0 kHz and 10.0 Hz were used for the experimental tests conducted on July 6, 2016 and July 13,2016, respectively.

2. Minimum-Euclidean Distance Detector for AOA Estimation

The previous system design uses the MLP neural network for AOA estimation [14]. This method has two drawbacks. First, the system needs to be retrained for different signal types and varying operational environments. The retraining interval can be as frequent as every 24 hours. Second, this form of estimation turns out to be computationally intensive and reduces the real-time performance of the overall system.

The recommendation of this thesis is to implement the AOA estimation using the minimum-Euclidean distance detector, where

$$\min\left\{d^2\left(\tilde{x},\tilde{s}_i\right)\right\} = \min\left\{\left\|\tilde{x}-\tilde{s}_i\right\|^2\right\}\ , \tag{1}$$

$\tilde{x}$ is the measured phase difference of the input signal vector and $\tilde{s}_i$ is a set of 181 basis vectors that represents the AOA from -90° to 90° with 1° resolution. The quantity $d^2\left(\tilde{x},\tilde{s}_i\right)$ measures the squared-Euclidean distance between the input vector and the set of basis vectors. In the absence of noise, the input signal vector matches exactly to one of the 181 basis vectors, and the AOA is the AOA represented by the basis vector. When noise is present, the minimum-Euclidean distance *d* provides the closest match to $\tilde{s}_i$ and its corresponding AOA. A partial mapping of the basis vectors is shown in Table 1.

Table 1. Partial Mapping of Basis Vectors $\tilde{s}_i$

AOA	S1	S2	S3
–90	0.003089	0.05508	0.01303
–89	0.003881	0.07475	0.01623
–88	0.001425	0.09788	0.01942
–87	0.002298	0.1279	0.02405
–86	0.005545	0.1661	0.02901
...			
86	0.002364	0.108	0.1035
87	0.000709	0.09708	0.08194
88	0.00193	0.08759	0.06509
89	0.002364	0.0845	0.0535
90	0.002364	0.08145	0.04555

In this chapter, the previous system design and its shortcomings were discussed. Several system enhancements were highlighted, including two major system overhauls: the redesign of the data acquisition architecture to provide deterministic data sampling and real-time post-processing, and the utilization of a unique encoding method to resolve the AOA ambiguities over the entire field of view of the DF antenna.

In next chapter, the system design for this thesis, the system calibration process, and the test setup used for data collection in the anechoic chamber is described.

III. SYSTEM DESIGN AND TEST SETUP

A detailed description of the new system design and the working principles of its components is provided in this chapter. The intricacies of how each component affects the system performance are explained, and the necessary calibration process for optimal system performance is outlined.

A. NEW SYSTEM ARCHITECTURE

The new system architecture for the photonic DF system is shown in Figure 3. The focus of this thesis is on photonic phase detection and signal post-processing for AOA estimation. Its components consist of the MZM, PD, DC-block, envelope detector, LNA, operational amplifier (Op Amp), and the signal processor.

Two key considerations for the design were:

1. Modularization of the optical segment and the RF segment to facilitate sub-system testing and troubleshooting, and
2. Improving the system portability and operational robustness for future out-field testing.

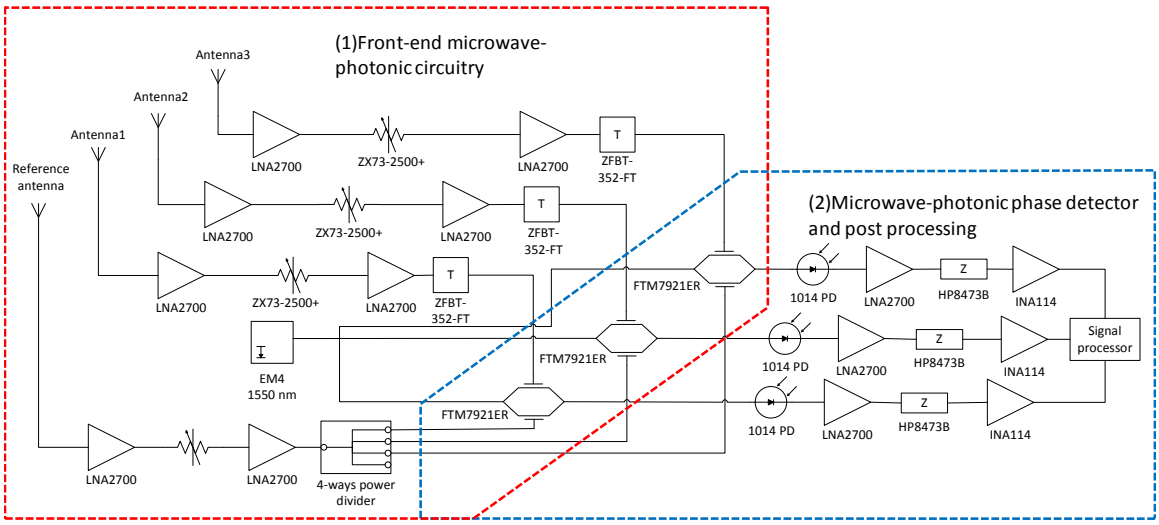

Figure 3. New System Architecture

B. COMPONENTS USED IN DF SYSTEM DESIGN

The front-end microwave photonic circuit design is detailed in [16]. The components described here begin with the MZM stage shown in Figure 4.

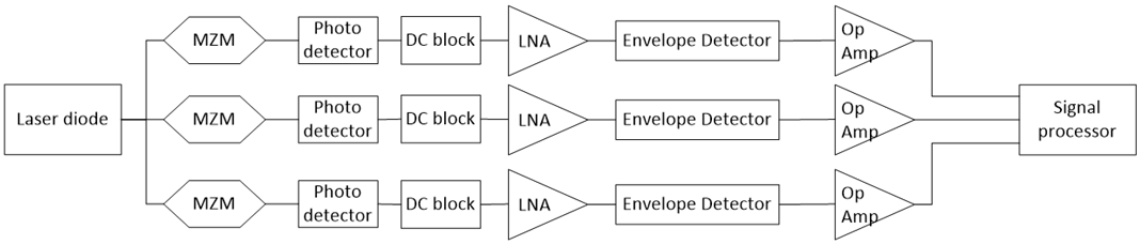

Figure 4. Photonic DF System Design (Back-end)

1. Mach-Zehnder Modulator

Early works on the MZM were established in [18], [19], and the invention of the MZM interferometer [20] enabled the modulation of a laser source by the splitting of laser energy via an input Y junction. A simplified illustration of the MZM is shown in Figure 5. As the laser source can be pulsed at extremely high frequencies (500 GHz–1 THz), the RF signals that are modulated onto the laser can be sampled at rates as high as 1 THz. This gives the MZM an enormous advantage over conventional DF systems in terms of real-time bandwidth.

Conceptually, the RF signals on the MZM electrodes generate an electric field that either retards or advances the laser traveling through the optical cavities of the MZM [21]. The result is a recombination of the laser signals that is either constructive or destructive depending on the phase difference of the RF input signals. For the MZM used in this system, when the RF input signals are exactly in-phase, the output is perfectly destructive, and if the RF input signals are 180° out of phase, the output has a response with maximum amplitude.

Among the variants of MZMs [22], the lithium niobate ($LiNbO_3$) MZM, FTM7921ER, shown in Figure 6, was selected for this system due to its high electro-optic coefficient that produces large phase shifts per unit of driving voltage applied at its

electrode. The drawback of $LiNbO_3$ technology is that it has a relatively high refractive index for microwave signals as compared to optical signals. This mismatch limits the maximum modulation frequency that the device can handle. To mitigate this constraint, silicon dioxide buffer layers are typically added to its internal waveguides to reduce the refractive index. The FTM7921ER MZM has a high extinction ratio of 20 dB, an insertion loss of < 6 dB, and an optical frequency response of 40-GHz [23].

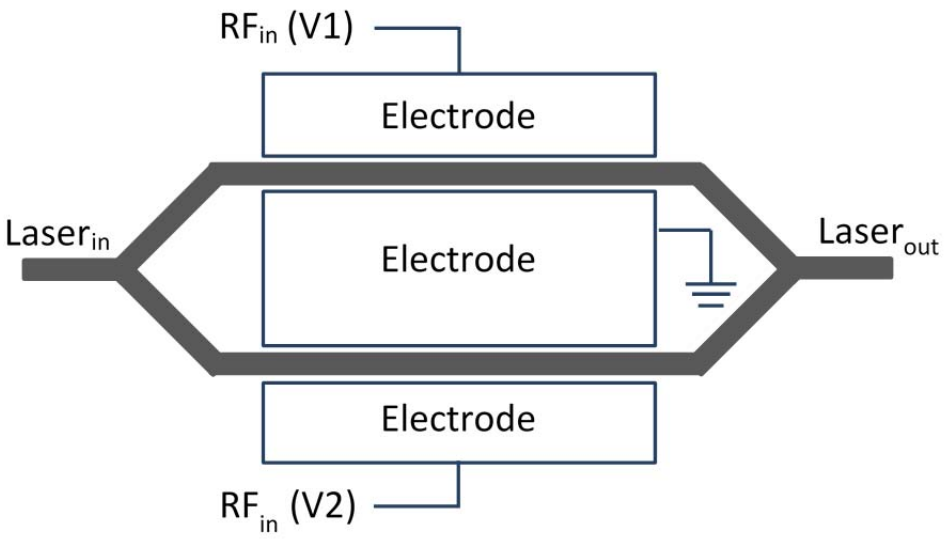

Figure 5. Schematic of the MZM

Figure 6. Actual $LiNbO_3$ MZM used in DF System. Source [23].

A brief overview of the MZM transfer function is presented to provide the background necessary for understanding the system calibration process as well as the system simulation, which is presented in Chapter IV.

First, we consider the electric field propagating in the two electrodes of the MZM given by

$$E_1 = A\sin 2\pi ft \tag{2}$$

and

$$E_2 = A\sin\left(2\pi ft + \phi\right), \tag{3}$$

where A is the field amplitude, f is the frequency, t is time and ϕ is the total phase difference between the two fields. The resultant output of the MZM is given by

$$E = E_1 - E_2 = A\sin 2\pi ft - A\sin\left(2\pi ft + \phi\right) \tag{4}$$

which can be rewritten using a trigonometric identity as

$$E = 2\cos\left(\frac{4\pi ft + \phi}{2}\right)\cos\left(\frac{\phi}{2}\right). \tag{5}$$

The output of the MZM consists of the product of two cosine expressions. The former is a high frequency component that is removed by the envelope detector in the subsequent stage, leaving the term

$$2\cos\left(\frac{\phi}{2}\right) \tag{6}$$

which is proportional to the phase difference between the RF signals at the two electrode arms of the MZM. A typical MZM transfer function is shown in Figure 7. The parameter V_π is the range of the transfer function, and V_{bias} is the offset voltage that is coupled onto the RF inputs to ensure that the system operates in the linear region of the MZM's transfer function.

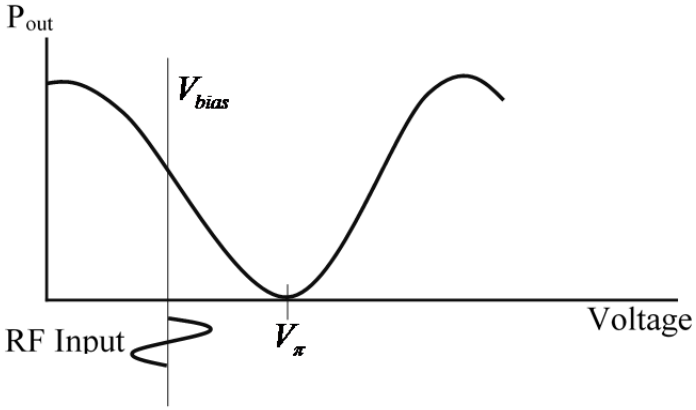

Figure 7. MZM Transfer Function

Two important conclusions can be drawn from the MZM transfer function. First, the amplitudes at the electrodes must match in order to produce an optimum output response from the MZM. Otherwise, the output electric field will contain a residual term that will corrupt the phase estimation of the RF signals. This is a key point to note during system calibration. Second, the phase difference between the RF signals can be determined by measuring the envelope amplitude of the MZM output, and consequently, the angle-of-arrival can be estimated. This concept is applied to the DF system simulation presented in Chapter IV.

2. Photo Detector

The conversion from the optical output of the MZM to electrical signal is performed by the New Focus 1014 ultra-high-speed PD, shown in Figure 8, and its detailed specifications are shown in Table 2. This is an InGaAs-based PD with good responsivity to the laser wavelength of 1550 nm used in the system. One drawback of using the PD is the high loss associated with the conversion process, as shown in Figure 9. The input power is 0.45 mW at 1.06 μm and produces an output of only –35 dBm. This implies a loss of almost 30 dB due to the optical to electrical conversion process; therefore, several stages of amplification were added after the PD to bring the signal to an appropriate voltage level for sampling and signal post processing.

Figure 8. New Focus 1014 PD. Source: [24].

Table 2. New Focus 1014 PD Specifications. Adapted from [25].

Active Diameter	12.0 µm
Wavelength Range	500-1630 nm
Optical Input	Singlemode FC
Responsivity	0.45 A/W
Rise Time	9.0 ps
Detector Material	InGaAs
Output Impedance	50.0 Ω
Bandwidth	45/40 GHz (typ/min)
Conversion Gain, Maximum	10.0 V/W
NEP	45.0 pW/√Hz
Power Requirements	Internal 9-V battery

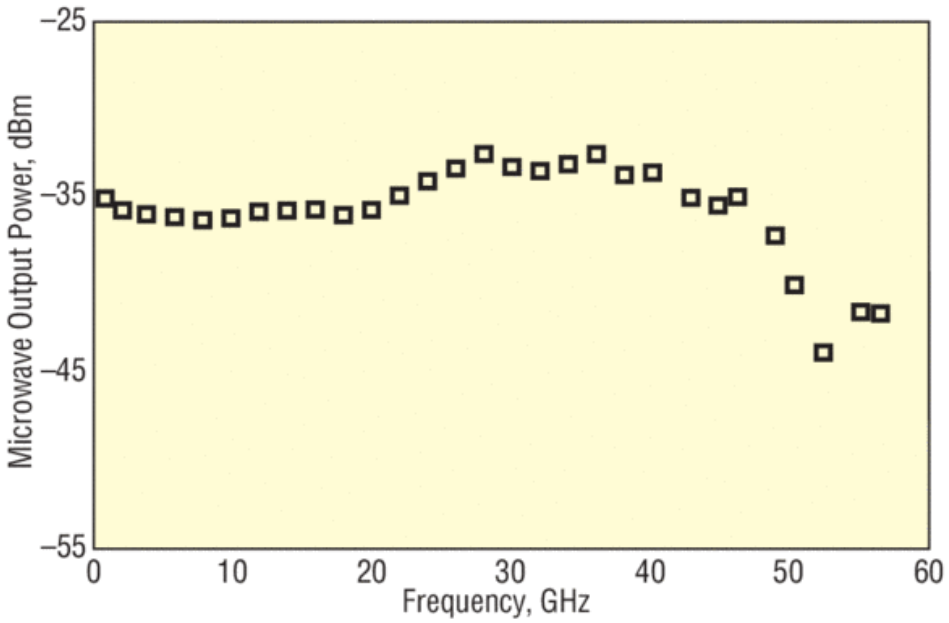

Figure 9. Frequency Response of New Focus 1014 PD. Source: [24].

3. Envelope Detector

The HP8473B envelope detector from Agilent is used to measure the envelope amplitude of the PD output. One key advantage of using this passive envelope detector is that external power sources are not required. This further simplifies the system design. It has an output impedance of 1.3 kΩ [26], which poses a problem for downstream components that are mostly designed to have an input impedance of 50.0 Ω. For proper impedance matching within the system, the INA114 operational amplifier is used as a buffer circuit to convert the high impedance output to a 50.0 Ω impedance output. Besides the impedance mismatch, the insertion loss of the envelope detector is also taken into account when designing the system.

C. SYSTEM CALIBRATION

Design for the RF front-end stage before the MZMs is detailed in [16]. The hardware components are modularized to separate the optical modules from the electrical modules. The purpose of this segregation is to allow ease of maintenance and calibration of equipment. The MZMs are packaged as shown in Figure 10, and the PD, DC block,

LNAs, envelope detector, and optical amplifiers are housed in a separate module shown in Figure 11.

Figure 10. MZM Modules with Inputs (blue RF cables) from the RF Front end

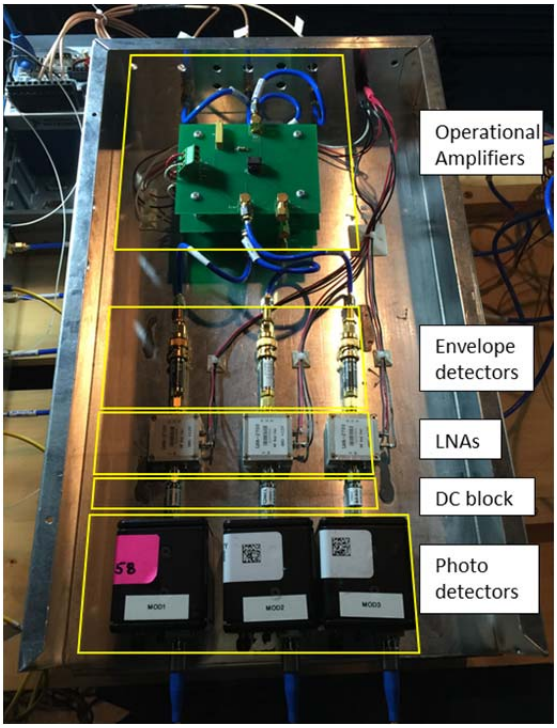

Figure 11. PD and Envelope Detector Modules with Optical Inputs from MZMs

Calibration of the system was performed in the optical laboratory prior to data collection and testing in the anechoic chamber. The entire calibration is divided into three stages. The first stage involves matching the transmission power of the front-end LNA stage right after the signals are received by the antennas. The calibration setup is shown in Figure 12. An HP83711B signal generator provides a 2.4-GHz CW calibration signal of 3 dBm at a distance of 5.7 m from the antenna sub-system. Details of the calibration results are captured in [16].

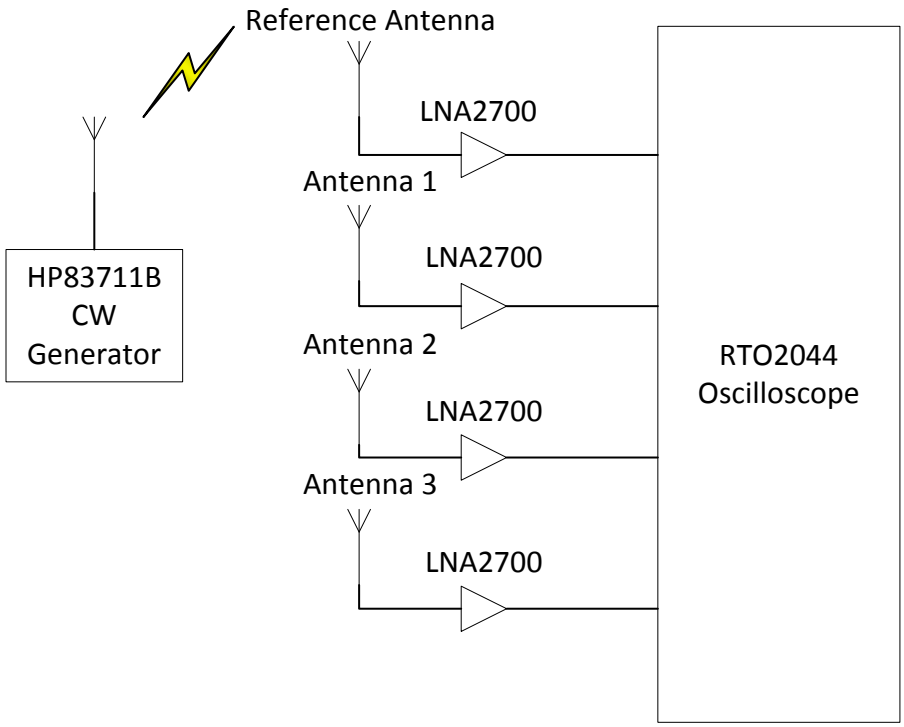

Figure 12. Calibration Setup for Front-end Antenna Sub-system

The second stage of calibration involves tuning of the voltage dividers for the attenuators and the T-bias to ensure that the RF signal power going into the MZM electrodes are matched. This is crucial to achieve an optimum response from the MZM as described by its transfer function. A typical matched response for all three MZM channels is shown in Figure 13, Figure 14, and Figure 15. Due to the non-linear characteristics of the RF and analog devices, identical power matching is not possible; however, laboratory results have demonstrated that an approximate matching is sufficient

for good system performance. This calibration only needs to be performed once as the response of the MZM is observed to be stable over the required operating power and temperature range.

In addition to the RF amplification calibration, the optical inputs to the MZMs must be calibrated for optimum optical response. Optical polarization tuning is required when connecting the high power 1550 nm DFB laser to optical input of the MZM as shown in Figure 16. Investigations have shown that the MZM optical input is polarization sensitive, and the input connectors should be tuned to match the optical output power of the MZM. Measurements for the optical input and output power for all three MZMs are shown in Table 3. According to the MZM datasheet, the insertion loss for the MZM is approximately 6 dB. This is consistent with the optical power response measured in Table 3.

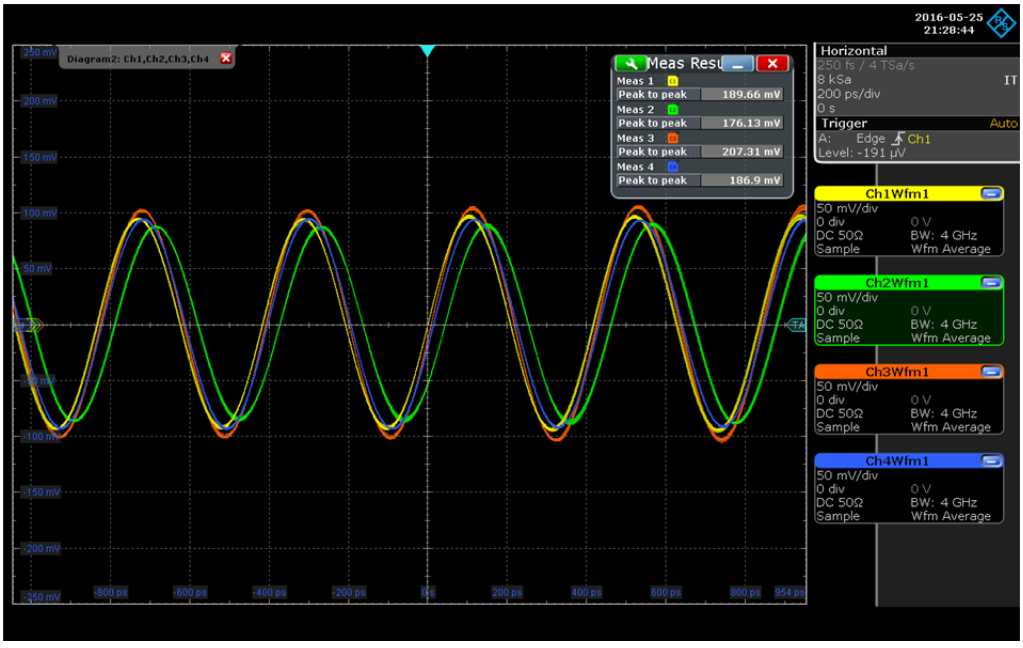

Figure 13. Matched Response for MZM#1: Ch1–Ch3 Are Signals from Reference Antenna, Ch4 Is Signal from Antenna1

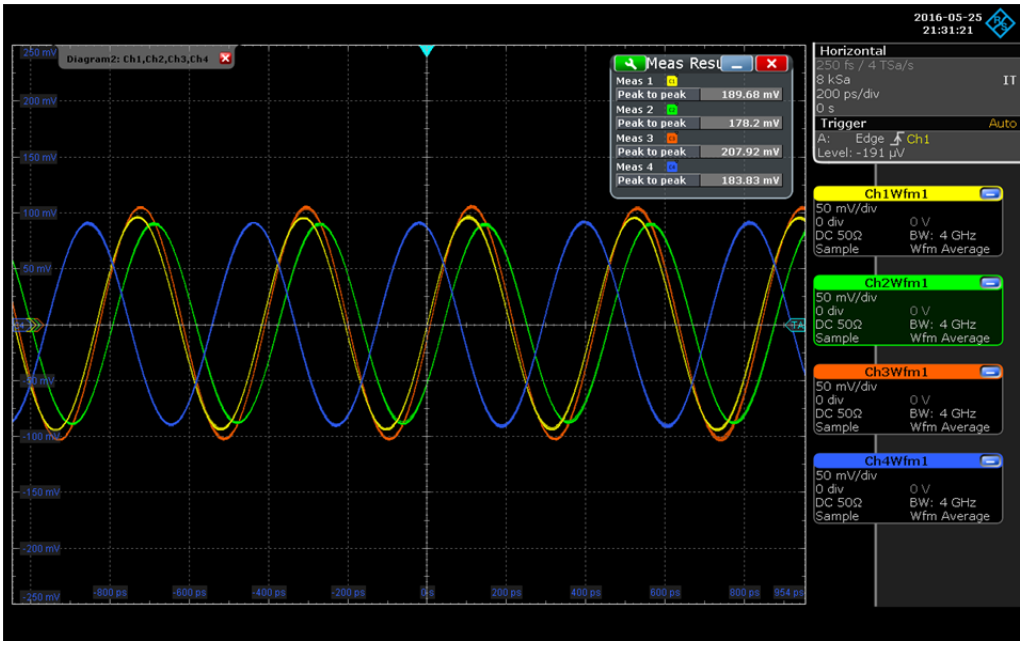

Figure 14. Matched Response for MZM#2: Ch1–Ch3 Are Signals from Reference Antenna, Ch4 Is Signal from Antenna2

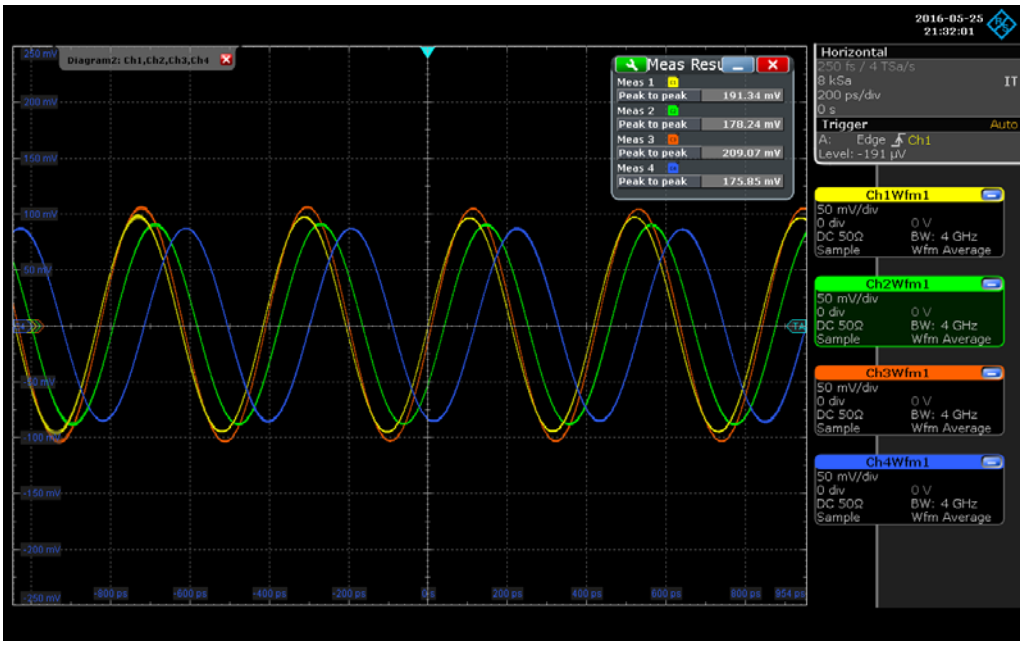

Figure 15. Matched Response for MZM#3: Ch1–Ch3 Are Signals from Reference Antenna, Ch4 Is Signal from Antenna3

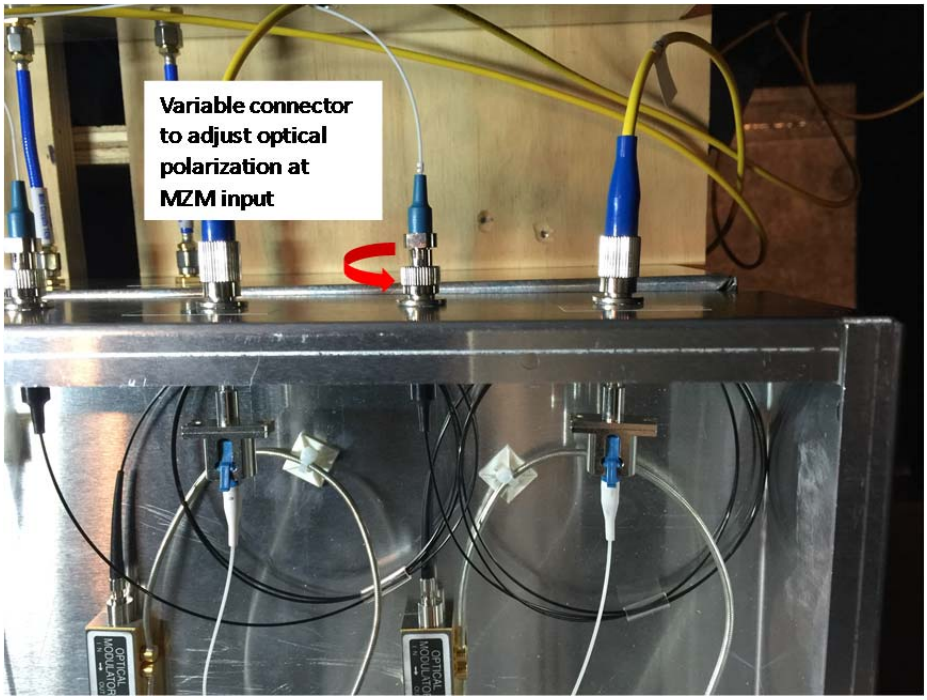

Figure 16. Variable Connectors to Adjust Optical Polarization at MZM Input

Table 3. Measured Optical Input and Output Power of MZMs

	Input Power (mW)	Output Power (mW)
MZM 1	22.1	5.45
MZM 2	20.5	5.42
MZM 3	26.4	5.61

D. SOFTWARE ARCHITECTURE DESIGN

The signal acquisition software was designed using Labview10 with Real-time module and FPGA module add-ons. Labview software is a graphical programming environment that allows quick prototyping systems to be developed on National Instruments hardware with minimal coding requirements. The graphical codes from the FPGA, cRIO controller, and the processing computer are shown in Figure 17, Figure 18, and Figure 19, respectively.

The sampling rate of the system was controlled by the ticks count input that determines the loop cycle time for the FPGA module. For this project, the FPGA was configured to run on a 40-MHz internal clock. Consequently, a tick count setting of 40000 provides a deterministic 1.0-kHz sampling rate for the system.

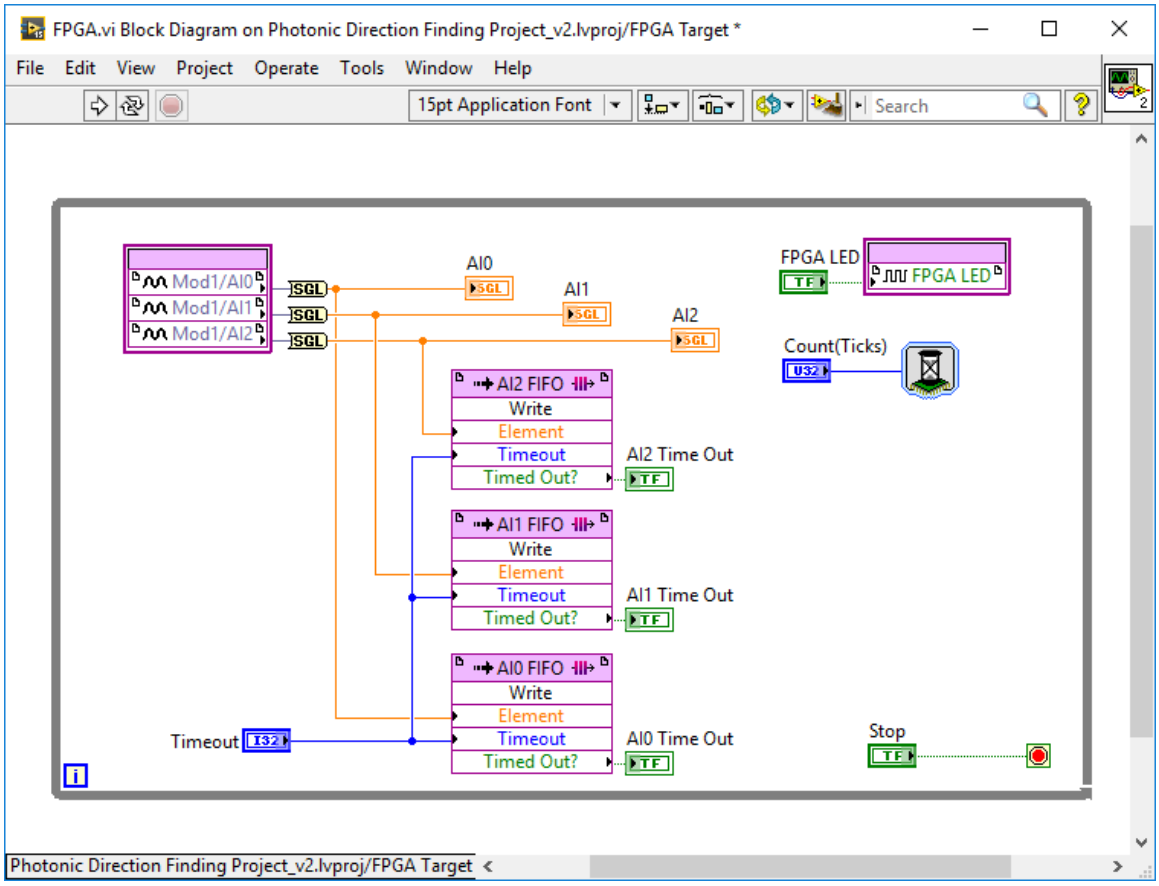

Figure 17. FPGA Code for DMA Transfer to cRIO Controller

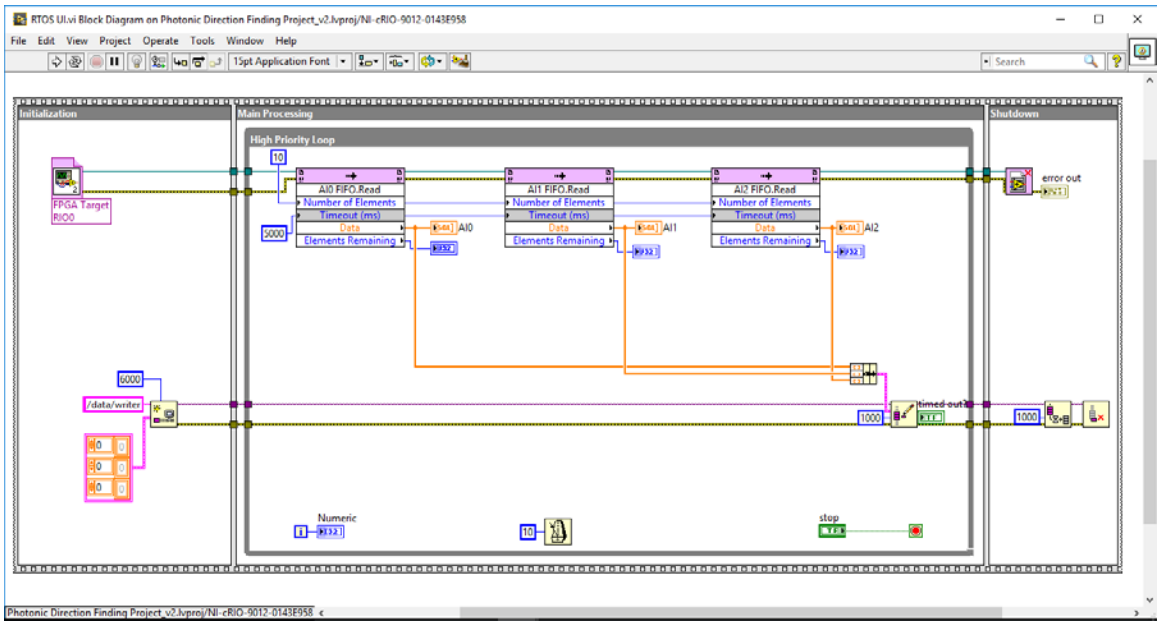

Figure 18. cRIO Controller Code to Read Sampled Data and Write to Processing Computer

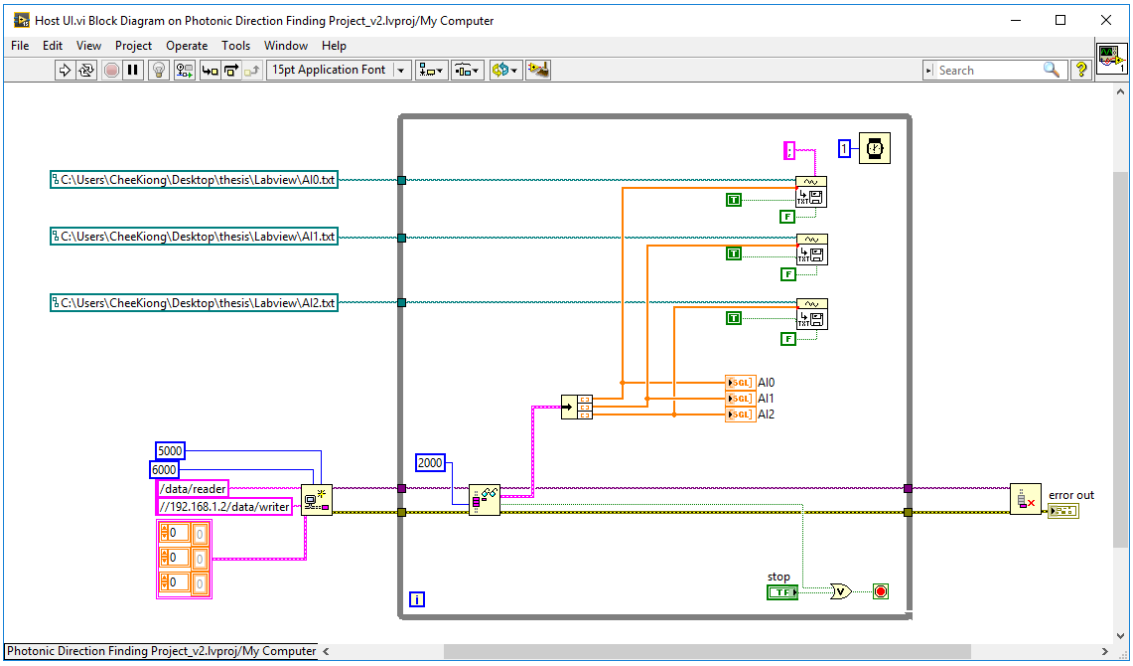

Figure 19. Processing Computer Code to Read Data from cRIO Controller via TCP Protocol

E. TEST EQUIPMENT

The following test equipment, provided by Rhode and Schwarz, was used for system testing in the anechoic chamber as well as for troubleshooting of the system in the laboratory environment:

1. SMW200A Vector Signal Generator with 100-kHz to 20-GHz operating frequencies
2. RTO2044 Oscilloscope with 4.0-GHz real-time bandwidth
3. FSW Spectrum analyzer with 2.0 to 26.5-GHz operating frequencies

The SMW200A Vector Signal Generator has up to 2.0 GHz of internal modulation bandwidth and is capable of generating a high quality digitally modulated signal required for system testing. This equipment was used to generate the linear FMCW and P4 signals at a carrier frequency of 2.4 GHz. The FSW spectrum analyzer was used to verify the signal waveform integrity. As shown in Figure 20, the linear FMCW has a carrier frequency of 2.4 GHz, a 100-kHz modulation bandwidth, and a modulation period of 100 ms.

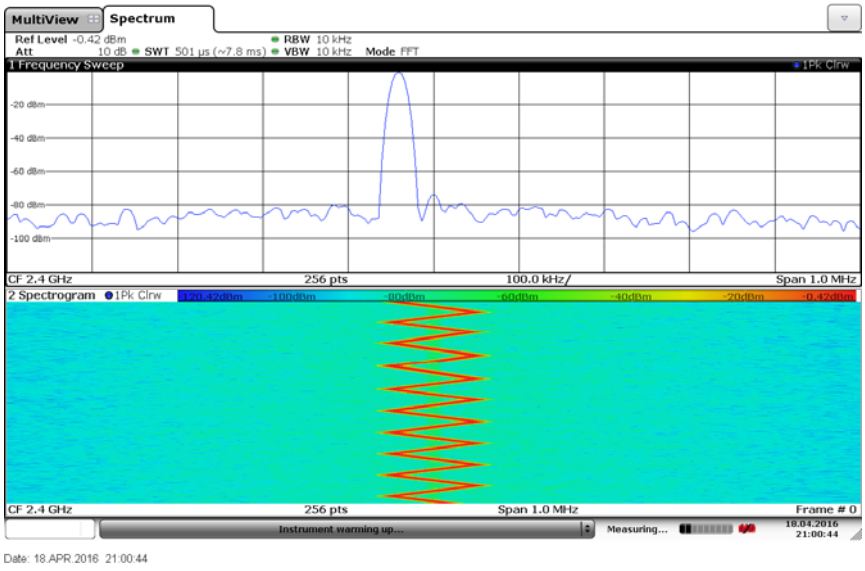
MultiView
Spectrum
Ref Level -0.42 dBm
Att 10 dB SWT 501 µs (~7.8 ms) RBW 10 kHz VBW 10 kHz Mode FFT
1 Frequency Sweep
1Pk Clrw
-20 dBm
-40 dBm
-60 dBm
-80 dBm
-100 dBm
CF 2.4 GHz 256 pts 100.0 kHz/ Span 1.0 MHz
2 Spectrogram 1Pk Clrw
-120.42dBm -100dBm -80dBm -60dBm -40dBm -20dBm -0.42dBm
CF 2.4 GHz 256 pts Span 1.0 MHz Frame # 0
Instrument warming up...
Measuring...
18.04.2016 21:00:44
Date: 18.APR.2016 21:00:44

Figure 20. Linear FMCW Signal with 100-kHz Modulation Bandwidth and a 100 ms Modulation Period

The RT2044 oscilloscope is another tool that is extremely useful for analyzing the intermediate signals within the DF system. Due to its 4-GHz real-time bandwidth, the test signals generated at 2.4 GHz can be analyzed without the need for any signal down-conversion. This greatly reduces the system analysis and troubleshooting effort. The oscilloscope was used to verify that the P4 signal contained phase changes occurring at the desired location on the signal waveform. An example of such real-time analysis is shown in Figure 21.

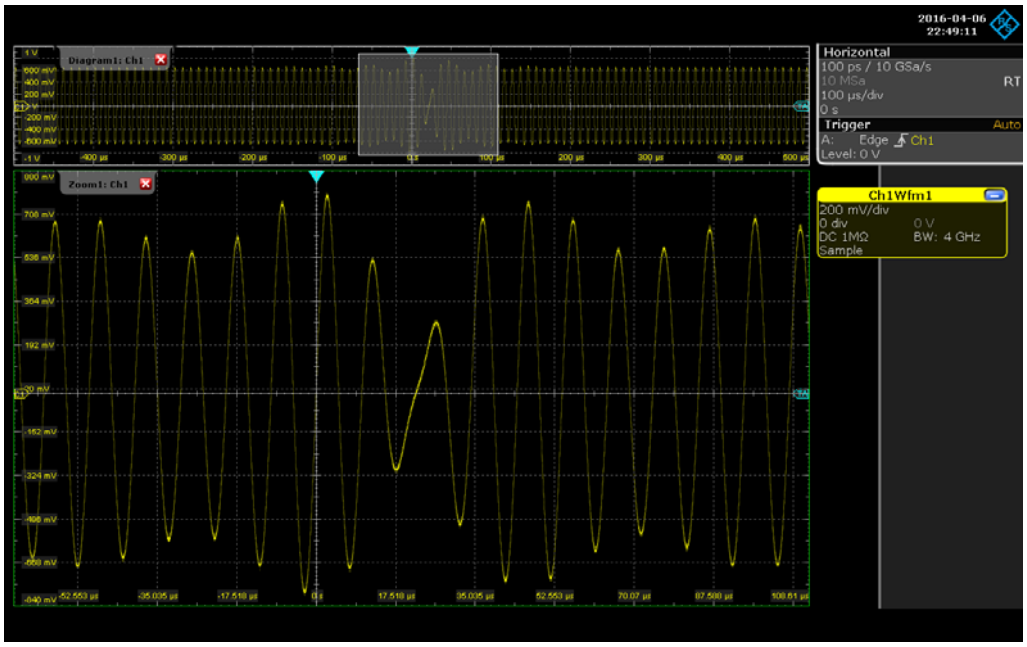

Figure 21. Phase Change in P4 Waveform Captured by RT2044 Oscilloscope

1. Test Setup

The system test was conducted at the Naval Postgraduate School in Monterey, California. The main facilities included the anechoic chamber and the optical lab located in Spanagel Hall. All tests in the anechoic chamber were conducted with the chamber fully enclosed to minimize interference from external sources and multipath propagation effects from the intended transmission source. The test setup in the chamber is shown in Figure 22 and Figure 23. Prior to the conduct of the tests, the system was calibrated to ensure that the signal power traversing each RF and optical path was matched. This was

crucial to the system AOA estimation performance as any mismatch in the signal power at the electrodes of the MZM results in a sub-optimal response, as described by the MZM transfer function in Chapter II.

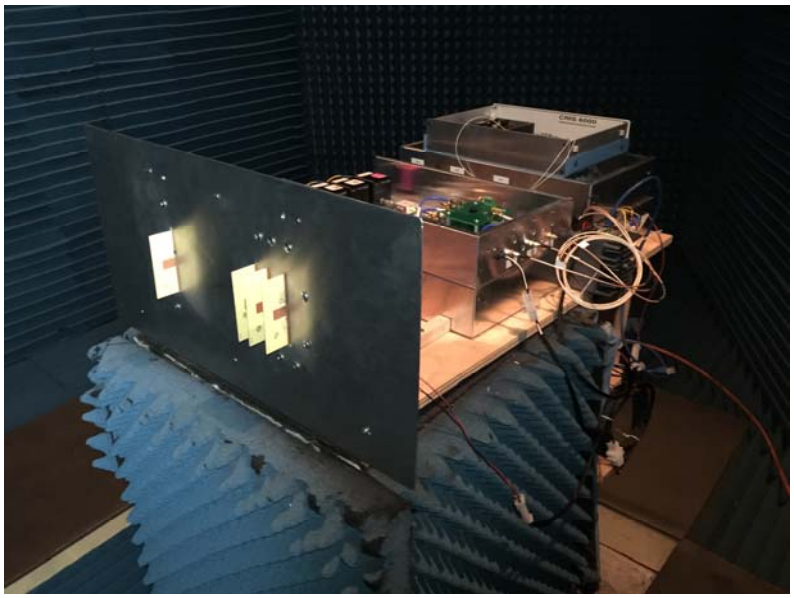

Figure 22. Photonic DF System in Anechoic Chamber

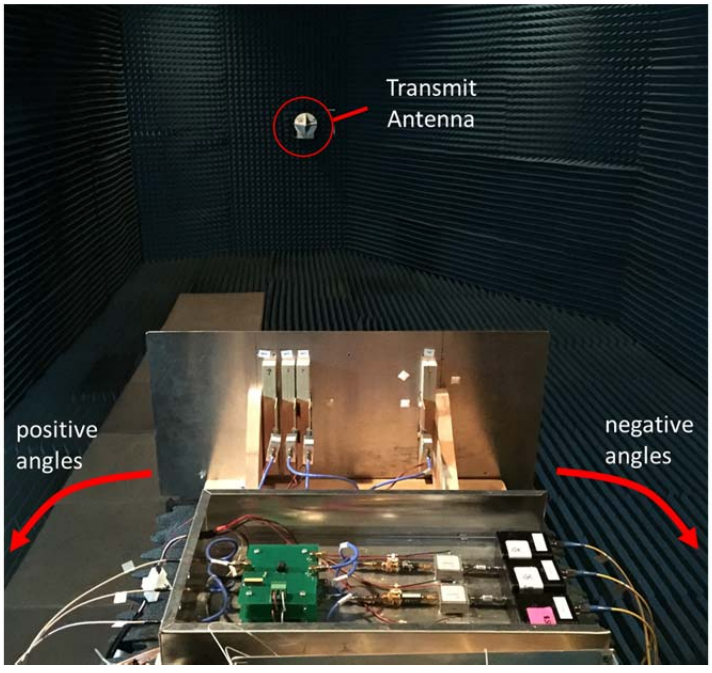

Figure 23. Transmission Antenna in Anechoic Chamber

2. Test Procedure and Data Collection

The location of the transmit antenna in the anechoic chamber is illustrated in Figure 23. It is located 5.7 m from the DF system with 0° referring to the angle when the antenna array is directly facing the transmit antenna. The negative angles and positive angles are defined by the red arrows shown in Figure 23. The transmitter is located directly outside the anechoic chamber and is turned on prior to performing the sweep cycle from –90° to +90°. The sweep is performed with 1° resolution, and the dwell time at each angle is approximately 3.5 s.

Testing of the system was conducted on two separate occasions, Test 1 on July 6, 2016, and Test 2 on July 13, 2016. Test 1 was conducted at a sampling rate of 1 kHz, while Test 2 was conducted at a sampling rate of 10 Hz. For both test sets, the same LPI signal parameters were used. The raw data were collected on a LENOVO ThinkPad T430 laptop with Intel Core i5 processor running the Windows 10 operating system, 8 GB of random access memory, and 500 GB of solid-state hard disk.

Although the data was collected in a highly controlled environment to minimize interference and RF propagation effects, it can be observed from Figure 24 that the raw data was corrupted with bad data points, possibly due to signals reflecting off the metallic structure of the system. Signal post-processing was performed to truncate the non-useful front and back portion of the data and to remove the bad data points during the sweep cycle.

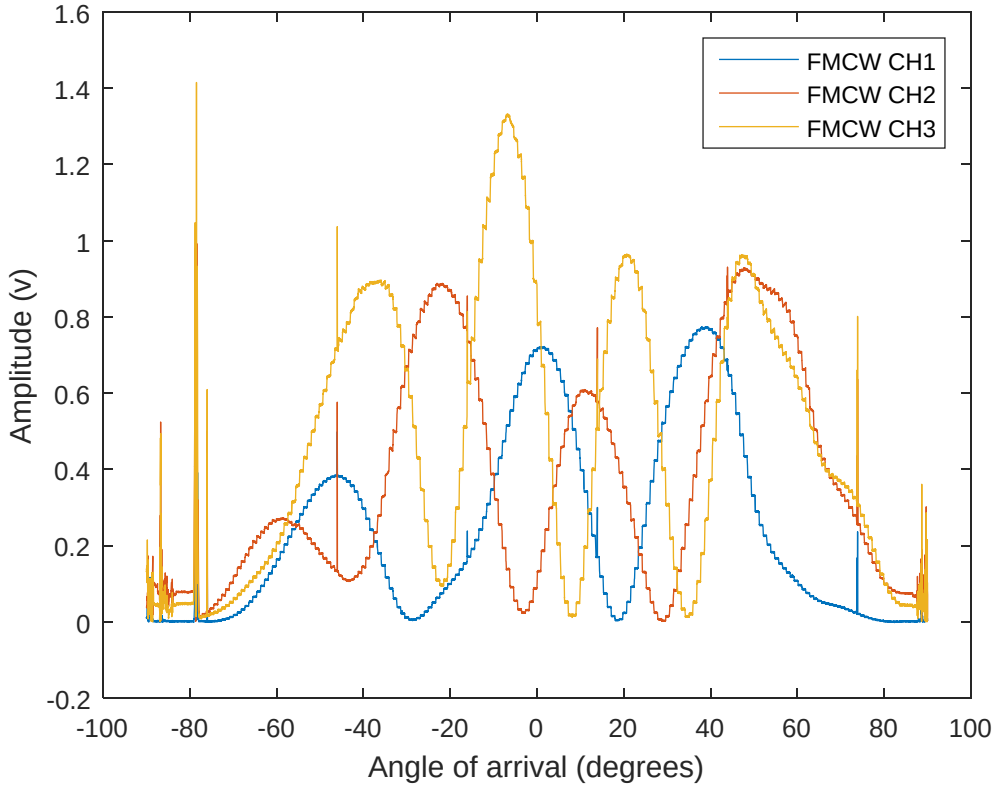

Figure 24. Raw FMCW Data Collected on July 6, 2016

In this chapter, the system design, system calibration procedures, and the experimental test setup and data collection process in the anechoic chamber were covered. The mathematical model for the MZM simulation is presented in the next chapter, and a full system simulation developed to verify the system response to LPI signals is described.

THIS PAGE IS INTENTIONALLY LEFT BLANK

IV. SYSTEM SIMULATION

The system simulation was carried out in two stages. First, the MZM was simulated, and the model was verified with laboratory results using the MZM hardware. Subsequently, simulated LPI signals were provided as input to the MZM model to ascertain that phase differences of the LPI signals are estimated accurately. In the second stage, the full DF system was simulated to evaluate the expected end-to-end system response when the AOA of the LPI signals were set to sweep from –90° to +90° with 1° resolution.

A. SIMULATION OF MZM

The dual-drive Mach-Zehnder Modulator is the most critical component for the photonic DF system. Each MZM in the photonic DF system accepts two RF signals, one from the reference antenna and the other from either antenna 1, antenna 2, or antenna 3. The MZM then produces a response based on the phase difference between the input signals. The transfer function for the MZM is [14]

$$T = \frac{1}{2}\left[1+\cos\left(\frac{V_1 - V_2}{V_\pi}\pi + \varphi_b\right)\right], \tag{7}$$

where V_1 and V_2 are RF signals applied to the MZM electrodes, V_π is the operating voltage range of the MZM to drive its output from the upper limit to the lower limit, and φ_b is the phase bias given by

$$\varphi_b = 2\pi\frac{\Delta_n}{\lambda} + \pi\frac{V_b}{V_\pi}, \tag{8}$$

where Δ_n represents the path lengths mismatch between the two input arms of the MZM, and V_b is the bias voltage on the input arms to ensure that the MZM operates in the linear region.

A MATLAB model was developed based on (7) for two primary purposes. First, the model was used to verify that the theoretical transfer function closely approximates the MZM characteristics and, second, to allow a back-of-the-envelope estimation of the expected response of the MZM for FMCW and P4 modulated signal. The latter can serve to predict whether the photonic DF system design is feasible for estimating the AOA for FMCW and P4 modulated signal.

By comparing the results shown in Figure 25, Figure 26, Figure 27, and Figure 28, we conclude that the MATLAB model matches well with the actual output from the MZM.

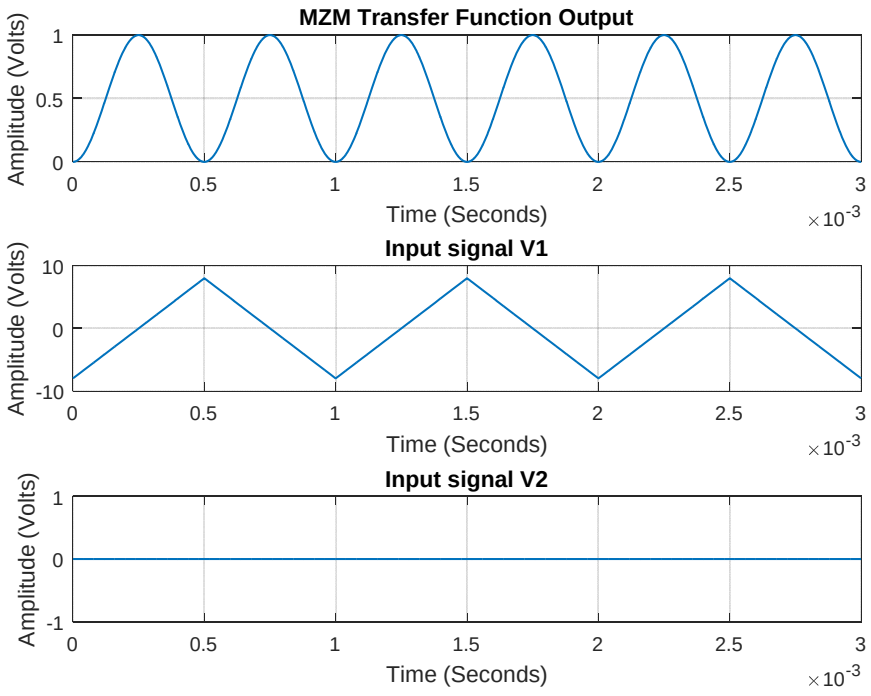

Figure 25. Simulated MZM Response for Saw-tooth Function

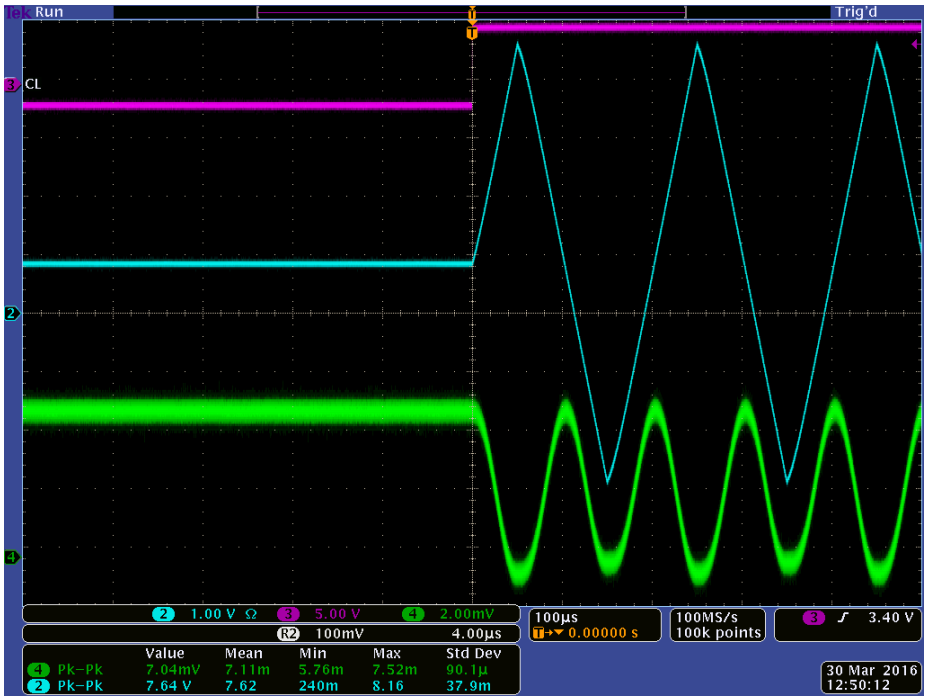

Figure 26. Actual MZM Response for Saw-tooth Function

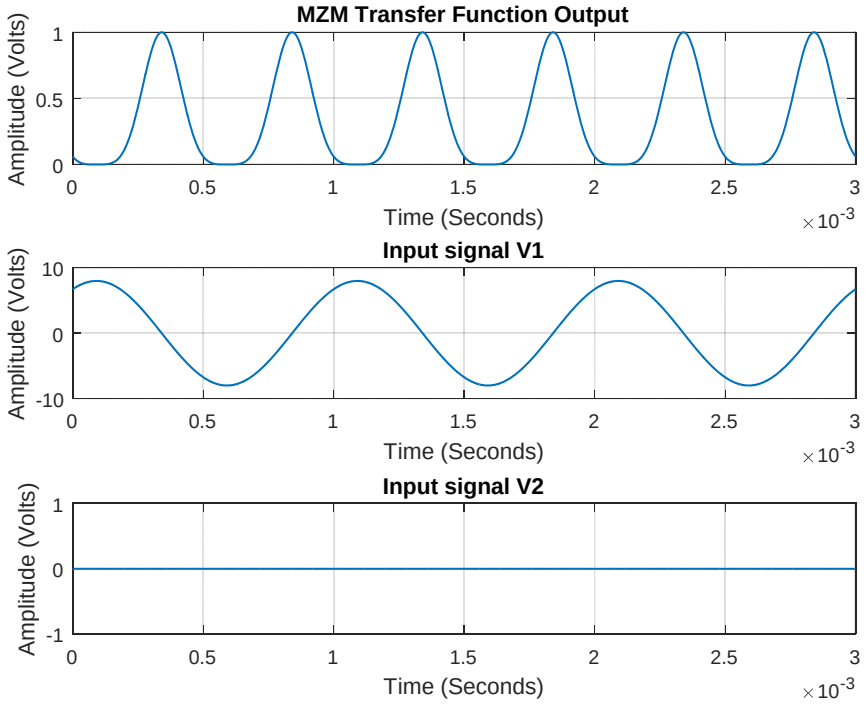

Figure 27. Simulated MZM Response for Sinewave Function

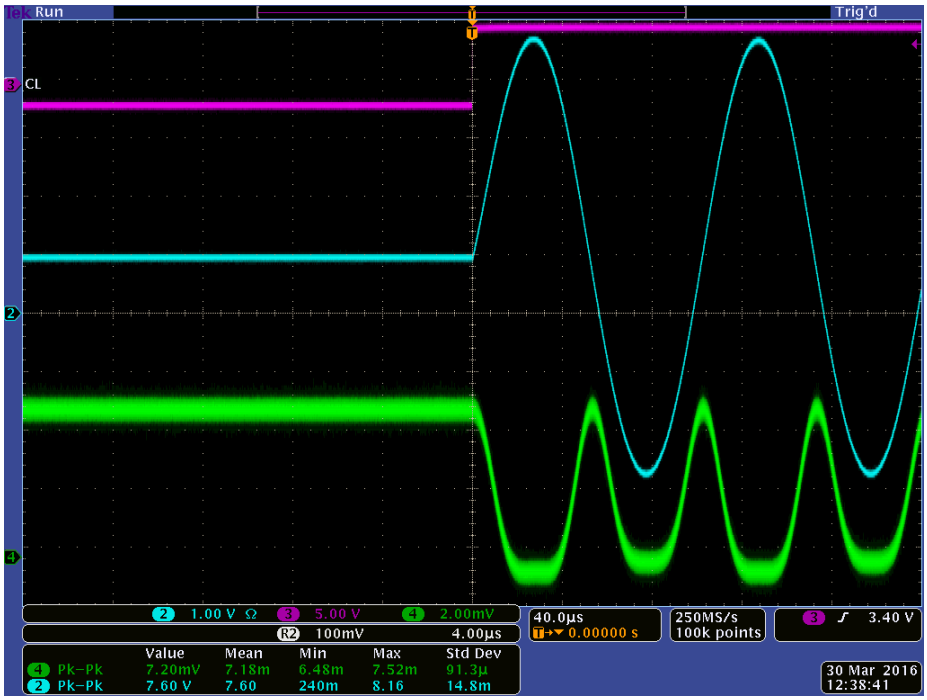

Figure 28. Actual MZM Response for Sinewave Function

Next, the MATLAB model was injected with the following LPI test signals:

1. FMCW signal at a 1.0-kHz carrier frequency with a modulation bandwidth of 500 Hz and modulation period of 20 ms. The simulations were done for the phase differences of 0°, 45°, and 90°.

2. P4 signal at a 1.0-kHz carrier frequency with 64 distinct phases and three cycles per phase. The simulations were done for the phase differences of 0°, 45°, and 90°.

The phase difference between the input signals is captured in the amplitude of the MZM output signal envelope. From Figure 29, Figure 30, and Figure 31, we observe that an increase in the phase difference between the FMCW signals entering the electrodes of the MZM results in a proportional increase in the envelope amplitude of the MZM output. Similarly, this result was demonstrated for P4 signal in Figure 32, Figure 33, and Figure 34. From the simulation, we conclude that the MZM is capable of measuring the phase difference of LPI signals with comparable results.

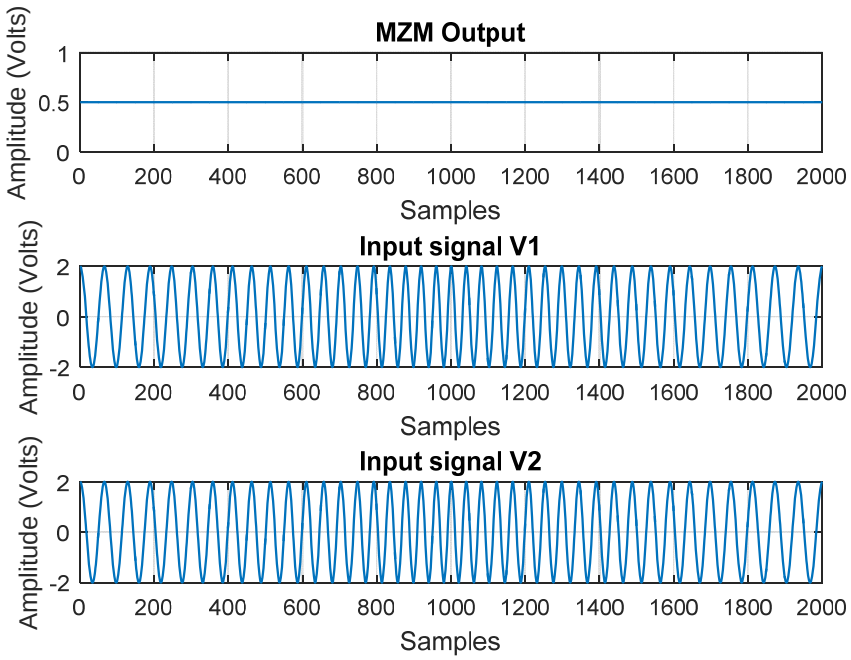

Figure 29. MZM Output for Linear FMCW Input with 0° Phase Shift

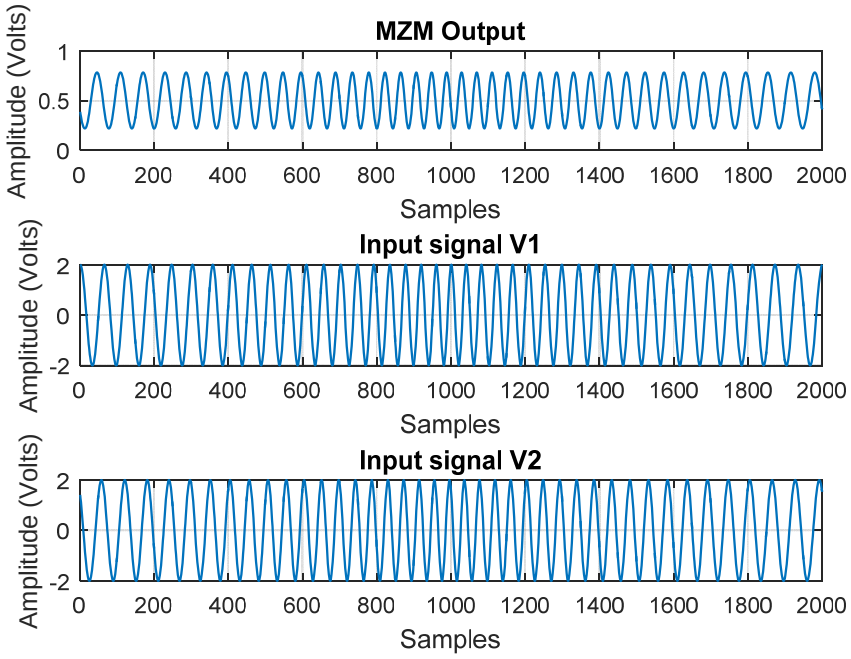

Figure 30. MZM Output for Linear FMCW Input with 45° Phase Shift

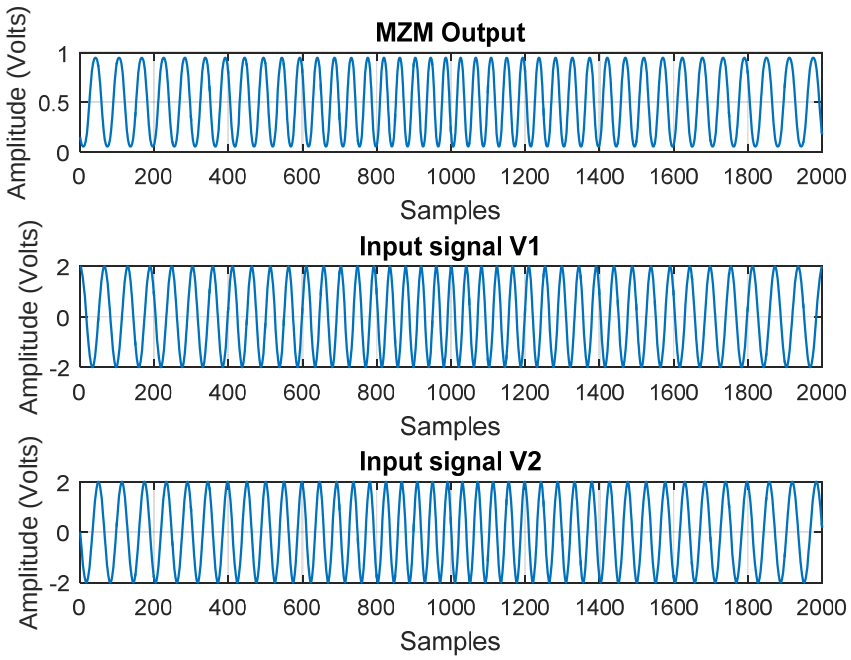

Figure 31. MZM Output for Linear FMCW Input with 90° Phase Shift

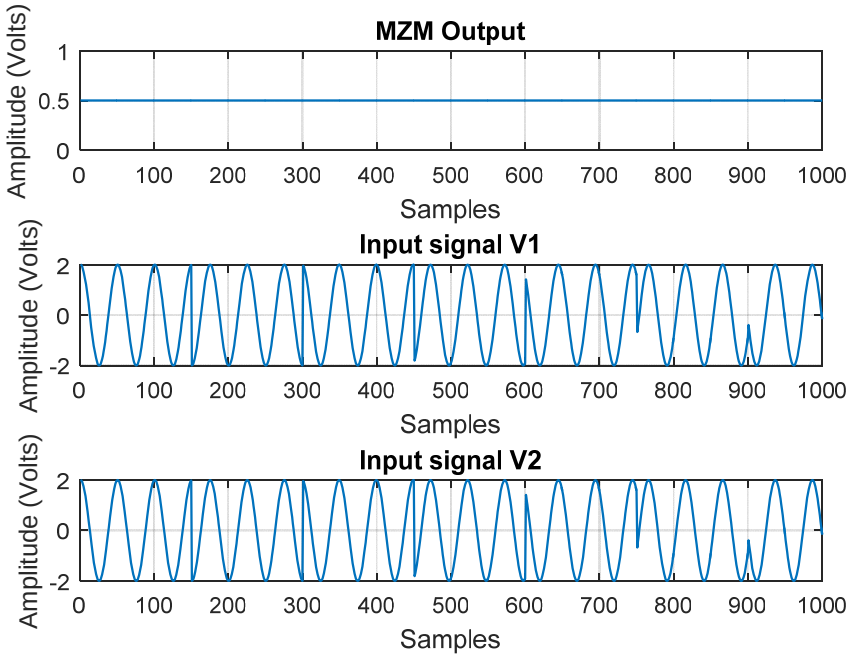

Figure 32. MZM Output for P4 Input with 0° Phase Shift

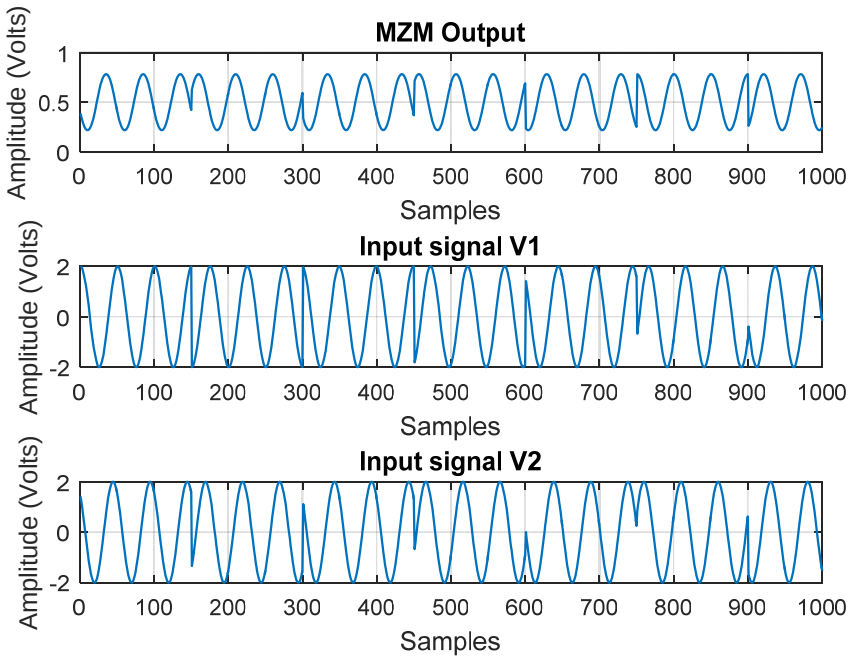

Figure 33. MZM Output for P4 Input with 45° Phase Shift

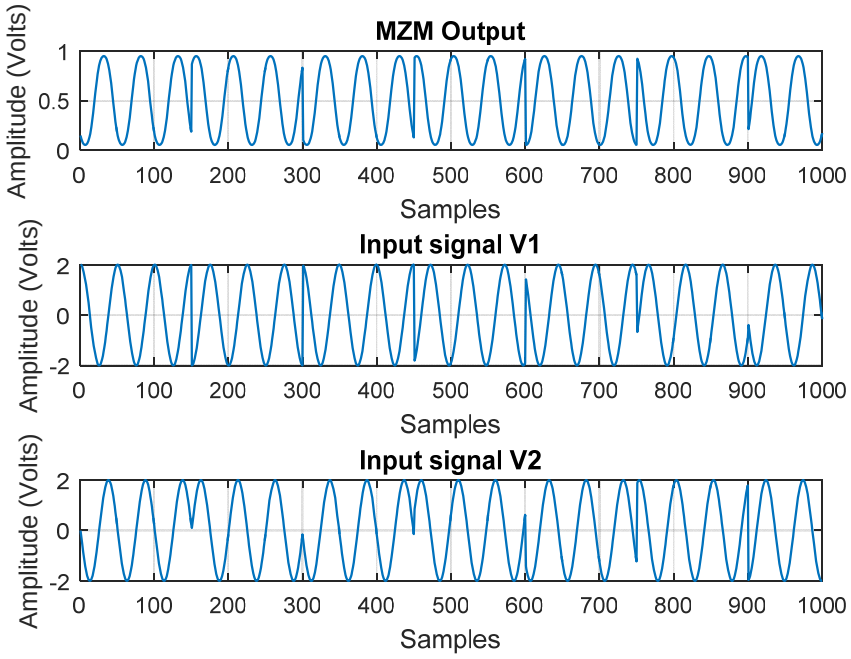

Figure 34. MZM Output for P4 Input with 90° Phase Shift

B. FULL SYSTEM SIMULATION

Following the verification of the MZM simulation, a full system simulation model was developed to analyze the theoretical system response of the photonic DF system. The model was injected with linear FMCW signal at 1.0-kHz carrier frequency with a modulation bandwidth of 500 Hz and modulation period of 20 ms, and the AOA was varied from –90° to +90° degrees with 1° resolution. The result from the simulation is shown in Figure 35. It can be observed that each degree step provides a set of three unique amplitudes that can be used for AOA matching in the signal processing stage. The AOA calculation is estimated using the minimum-Euclidean distance detector. It should be noted that the simulation gives an ideal response and does not take into account the non-linear characteristics of the system components such as the antenna array mutual coupling and MZMs. Nevertheless, the simulation model serves as an adequate approximation of the actual system response as can be seen in Chapter V.

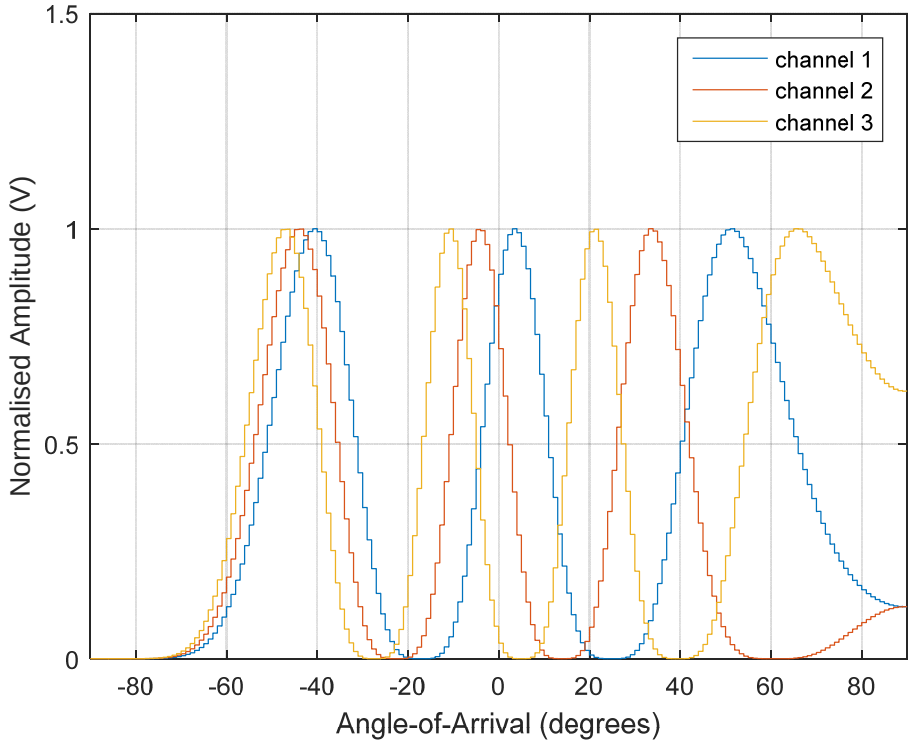

Figure 35. Simulated Response of DF System with Linear FMCW Signal

The system simulations provided a good estimation for the expected system response given an LPI signal input. It also helped to ascertain the performance of the system design at the theoretical level. The MATLAB codes for the software simulations are attached in the appendix.

In the next chapter, we describe experimental tests using linear FMCW and P4-coded signals carried out in the anechoic chamber and the signal post processing performed to analyze the system accuracy performance.

THIS PAGE IS INTENTIONALLY LEFT BLANK

V. TEST RESULTS

Experimental tests were carried out in the anechoic chamber to ascertain the system performance for specific LPI signal inputs. The tests were conducted in an anechoic chamber on the 6th floor of Spanagel Hall, at the Naval Postgraduate School. The system was calibrated prior to data collection, and test results for FMCW and P4 signals were collected on two separate occasions. The first test was conducted on July 6, 2016, and the second test was conducted on July 13, 2016.

The parameters for the LPI signals were as follows:

1. P4

   - Carrier frequency = 2.4-GHz
   - 6400 samples were generated on a 200-MHz clock rate (maximum supported clock rate of signal generator)
   - Number of unique phases, Nc = 64. There are 100 samples to represent each phase, and the phase period is 0.5 μs
   - The number of carrier cycles for each phase value, cpp = 120

   The baseband signal is shown in Figure 36.

2. FMCW

   - Carrier frequency = 2.4 GHz
   - Modulation bandwidth = 100 kHz
   - Modulation period = 100 ms

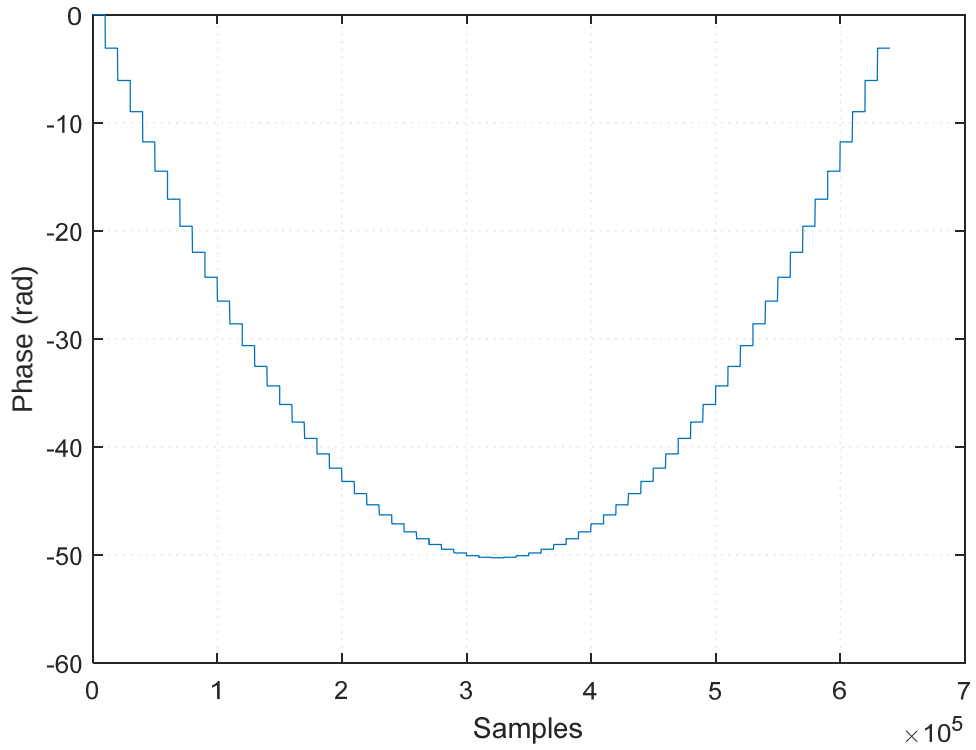

Figure 36. Phase Representation of P4 Signal Used for Experimental Tests

A. P4 TEST RESULTS

The first test on P4 signals was conducted on July 6, 2016.

The raw data collected was corrupted by system non-linearities due to signals reflecting off the surfaces of the system as the pedestal performed sweeps from –90° to +90°. The signal post processing removed the corrupted signals and performed truncation to extract only the raw data that represented the full sweep cycle. The result of the raw data collected, after normalization, is shown in Figure 37.

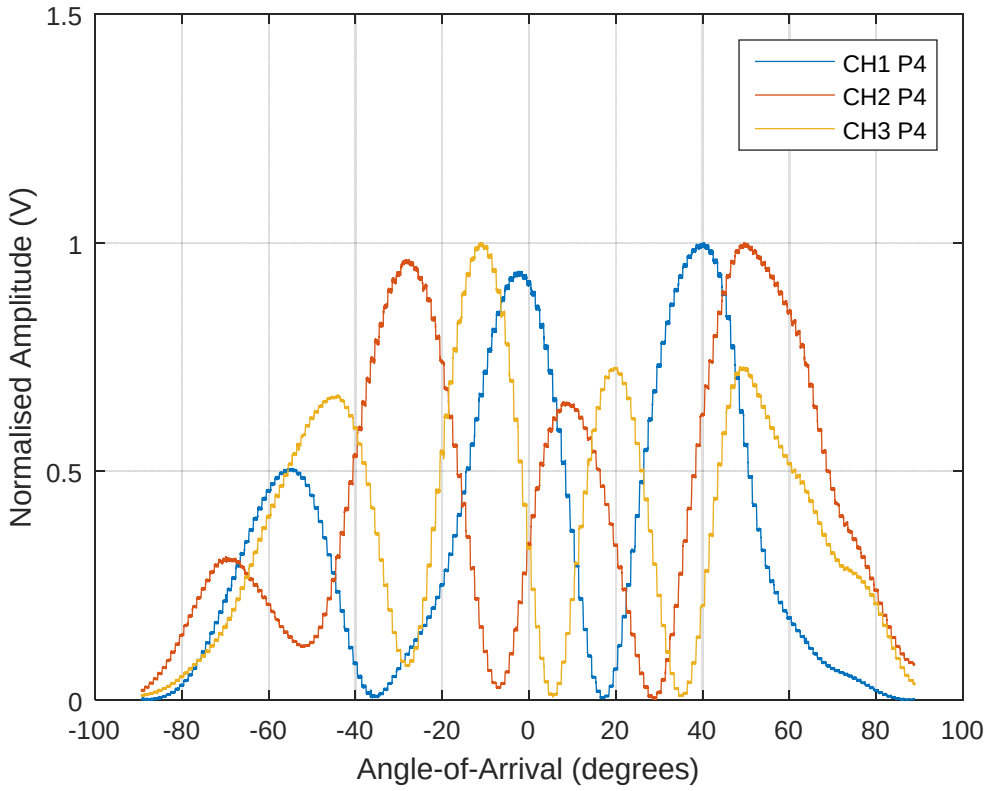

Figure 37. P4 Data after Post-processing and Normalization (July 6, 2016)

AOA estimation was accomplished by injecting the raw data through the minimum-Euclidean distance detector. The AOA estimation shown in Figure 38 demonstrates the system capability to perform DF on P4 signals. From Figure 39, the RMS error is 0.3205°. We also observe that the system has a tighter error bound between –45° to +45° and a larger error bound as the AOA tends toward the end-fire limits of –90° and +90°.

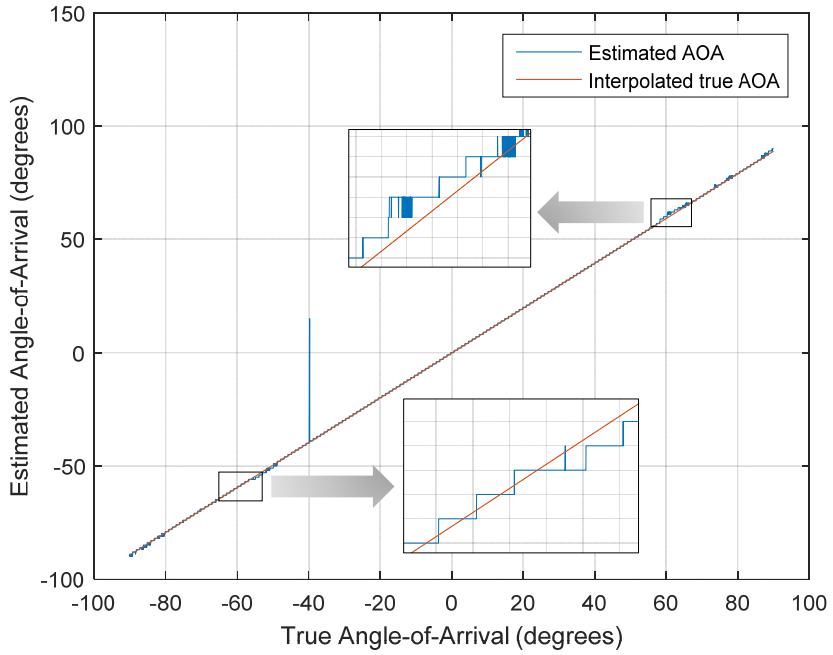

Figure 38. P4 AOA Estimation for Angle Sweep from –90° to +90° (July 6, 2016)

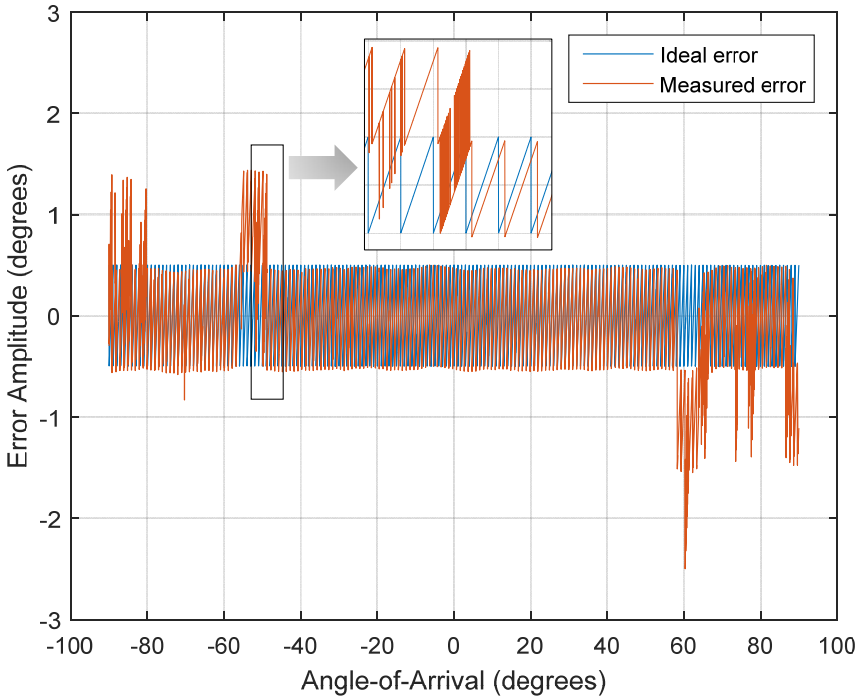

Figure 39. P4 Signal Error Plot (July 6, 2016)

The second test on P4 signals was conducted on July 13, 2016. The post processed and normalized data is shown in Figure 40. From the AOA estimation plot in Figure 41, we observe that there are more outliers present in this set of data. It also demonstrates that the AOA estimation nearing the end-fire angle of –90° and +90° tends to be less reliable. As shown in Figure 42, an RMS error of 0.8467° was measured for this run.

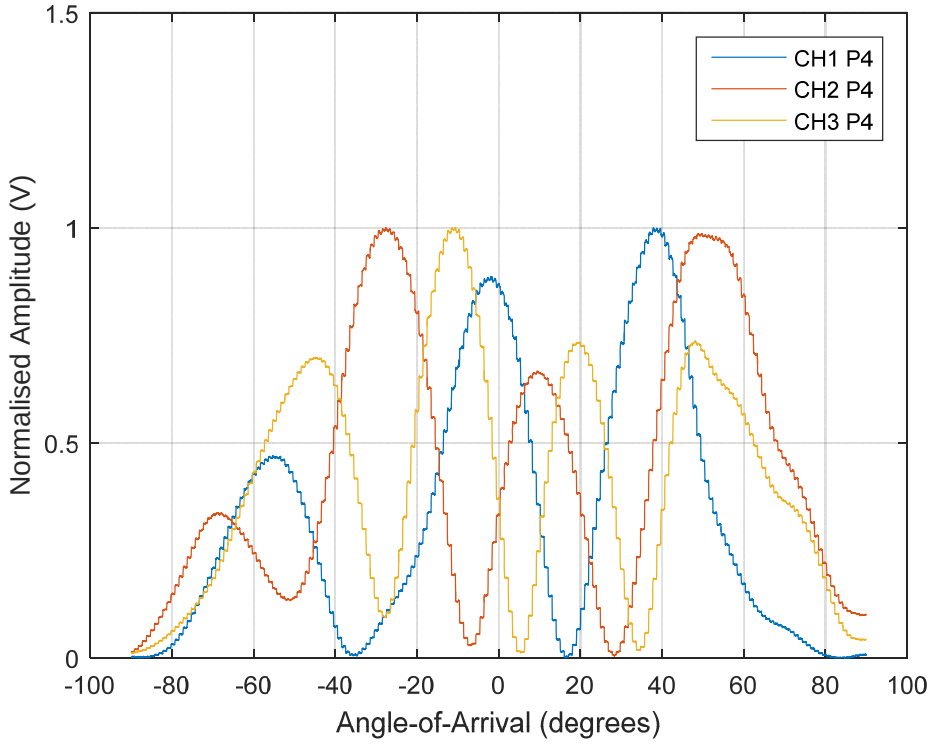

Figure 40. P4 Data after Post-processing and Normalization (July 13, 2016)

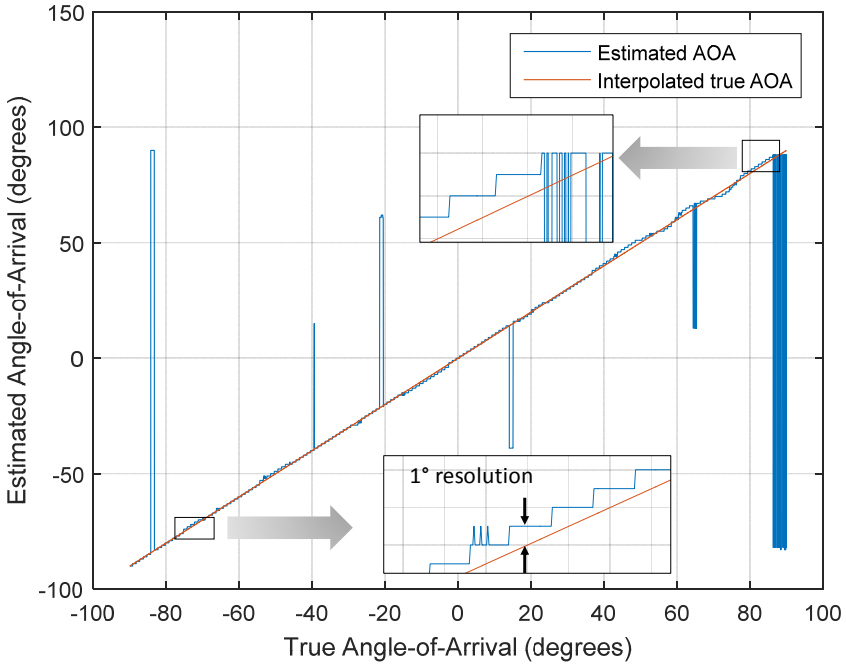

Figure 41. P4 AOA Estimation for Angle Sweep from –90 to +90 (July 13, 2016)

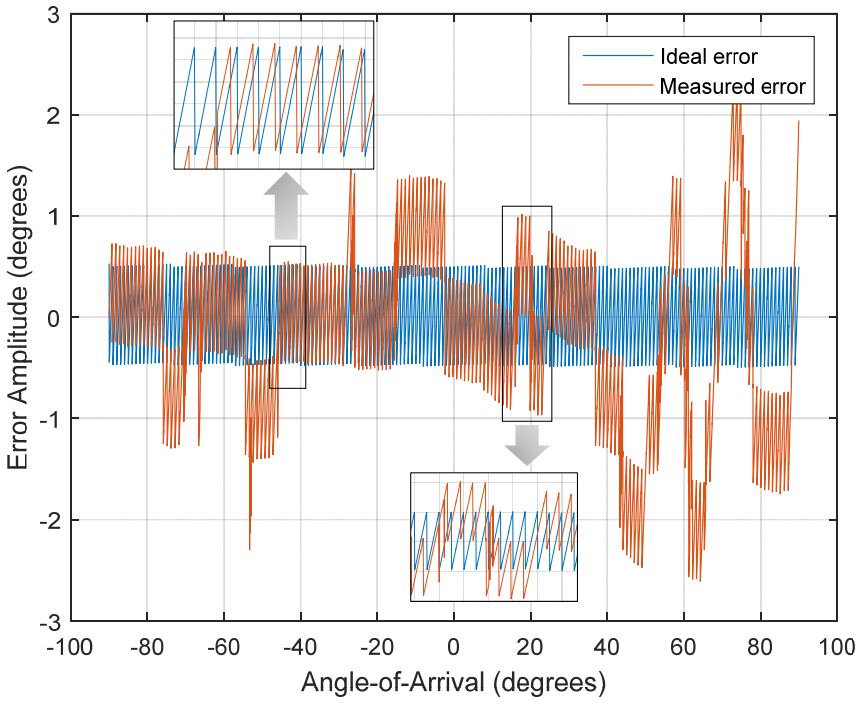

Figure 42. P4 Signal Error Plot (July 13, 2016)

B. FMCW TEST RESULTS

The first test on FMCW signals was conducted on July 6, 2016, and the post processed data is shown in Figure 43.

The AOA estimation shown in Figure 44 demonstrates the system capability to perform DF of FMCW signals. As shown in Figure 45, the RMS error was calculated to be 0.2904°. We also observe that the system has a relatively tight error bound between –80° to +80° and a larger error bound as the AOA tends toward the end-fire limits of –90° and +90°. This conclusion remains consistent with the data collected for P4 signals.

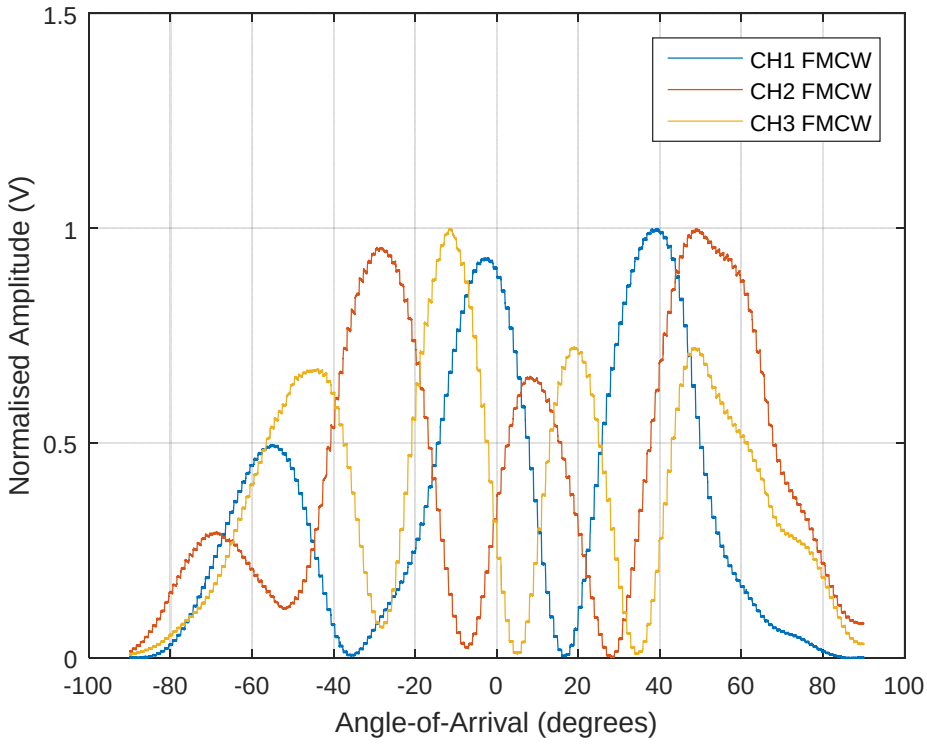

Figure 43. FMCW Data after Post-processing and Normalization (July 6, 2016)

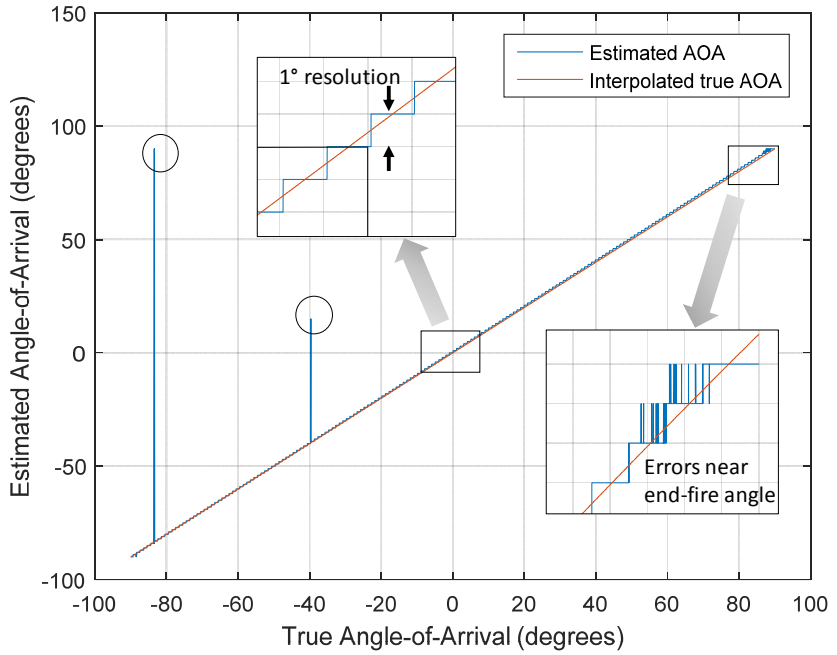

Figure 44. FMCW AOA Estimation for Angle Sweep from –90° to +90° (July 6, 2016)

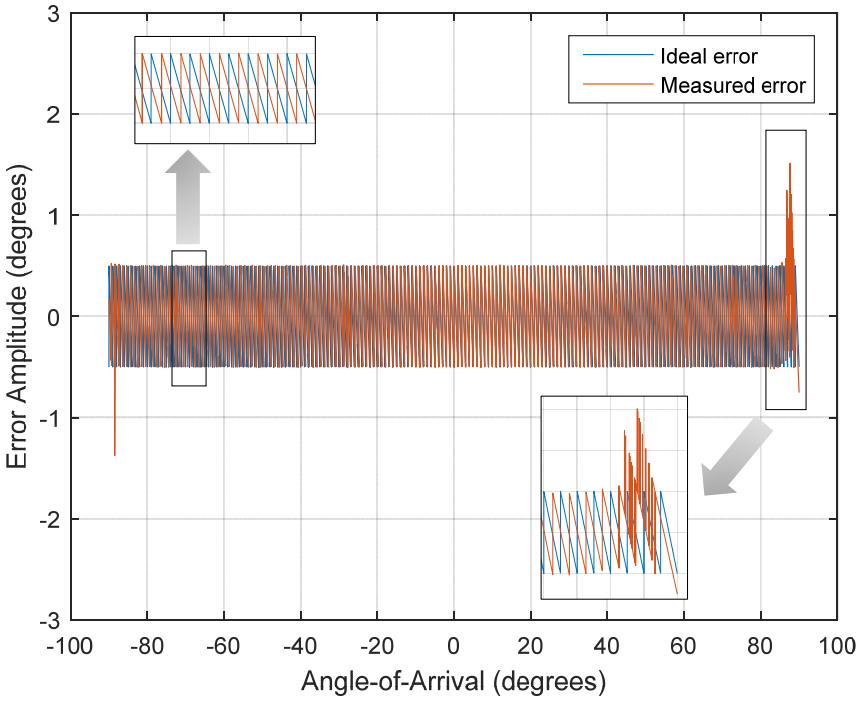

Figure 45. FMCW Signal Error Plot (July 6, 2016)

The second test on FMCW signals was conducted on July 13, 2016, and the post-processed data is shown in Figure 46. The AOA estimation shown in Figure 47 demonstrates the system capability to perform DF of FMCW signals. As shown in Figure 48, the RMS error was calculated to be 0.779°. We also observe that the system has a relatively tight error bound between –80° to +80° and a larger error bound as the AOA tends toward the end-fire limits of –90° and +90°. This is consistent with the data collected for P4 signals.

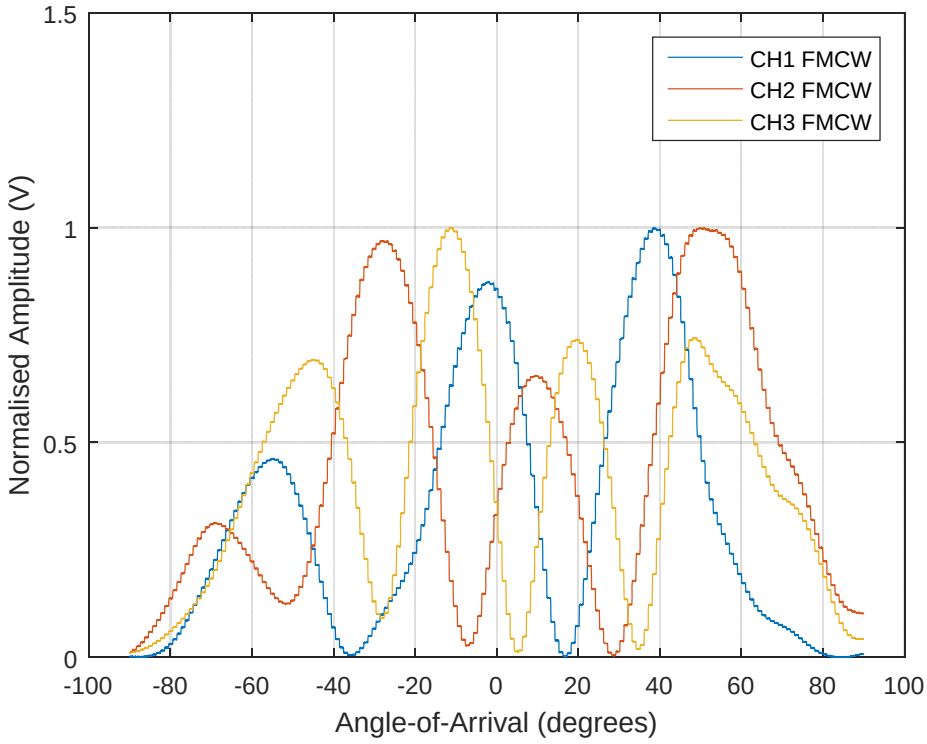

Figure 46. FMCW Data after Post-processing and Normalization (July 13, 2016)

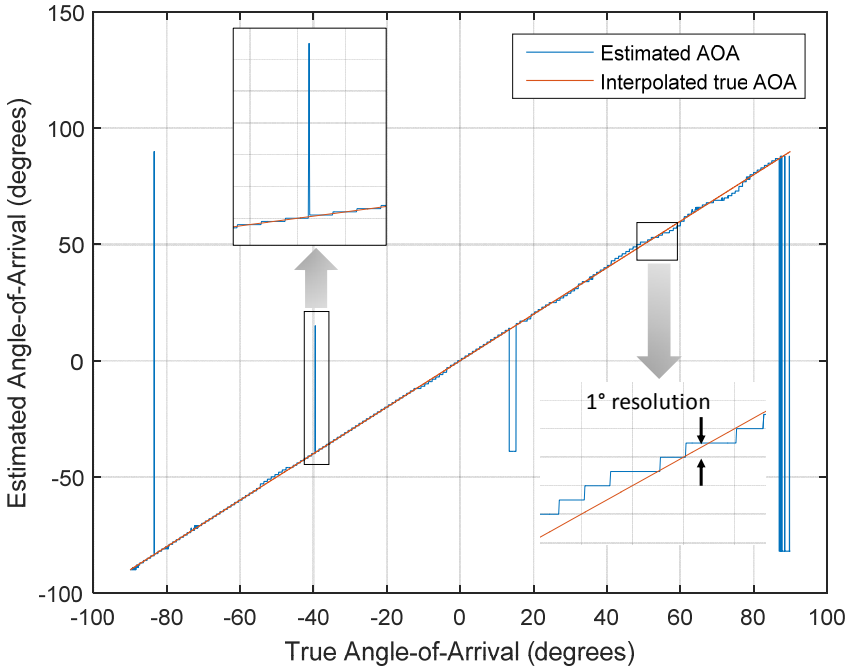

Figure 47. FMCW AOA Estimation for Angle Sweep from –90 to +90 (July 13, 2016)

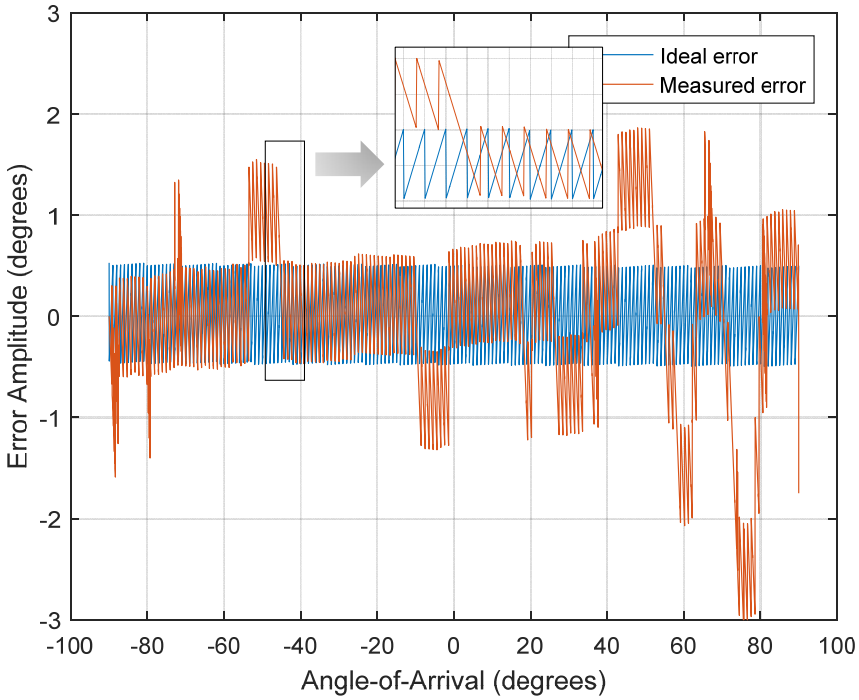

Figure 48. FMCW Signal Error Plot (July13, 2016)

As shown in the test data summarized in Table 4, the system is able to perform AOA estimation of P4 and FMCW signals with an RMS error less than 1° and standard deviation less than 1°. The measurements were taken one week apart with calibration performed once on July 6, 2016. This demonstrates the robustness of using minimum-Euclidean distance detection for AOA estimation.

Table 4. Result Summary of Tests Conducted

Test data	P4		FMCW	
	RMS error	STD	RMS error	STD
July 6, 2016	0.3205°	0.3205°	0.2904°	0.2904°
July 13, 2016	0.8467°	0.8329°	0.779°	0.779°

C. ANALYSIS OF OUTLIERS DATA

In this section, the outlier data for FMCW and P4 is analyzed to identify the source of error. Appropriate mitigation measures are also suggested for future research on the system.

1. P4 Outlier Data Collected on July 6, 2016

The outlier data was sampled from the estimated angle-of-arrival as shown in Figure 49. The zoom-in view of the outlier data is shown in Figure 50. Henceforth, only the zoom-in view of the outlier data is shown for subsequent signals analyzed. Twelve outliers are identified, and their sample numbers correspond to the range #17858 through #17869, respectively. The input raw data that correspond to the sample range are shown in Figure 51. These raw samples should rightfully give an AOA estimate between –39° and –40° instead of 15° as shown in Figure 52. To understand why the AOA was estimated incorrectly, we selected two of the outliers and calculated their minimum Euclidean distance AOA of –39°, –40°, and 15°. The results are shown in Table 5. We observed that these outliers have minimum-Euclidean distances matched to an AOA of 15°. This analysis demonstrates that the DF system design would give a possible erroneous AOA estimation for an angle resolution less than 1°. The same phenomenon was also observed, but not fully investigated, in [14].

Table 5. Minimum-Euclidean Distance Calculations for Outliers #17866 and #17869

Angle (degrees)	Minimum-Euclidean distance	
	#17866	#17869
–39	0.00136	0.00188
–40	0.00157	0.00126
15	0.00076	0.00073

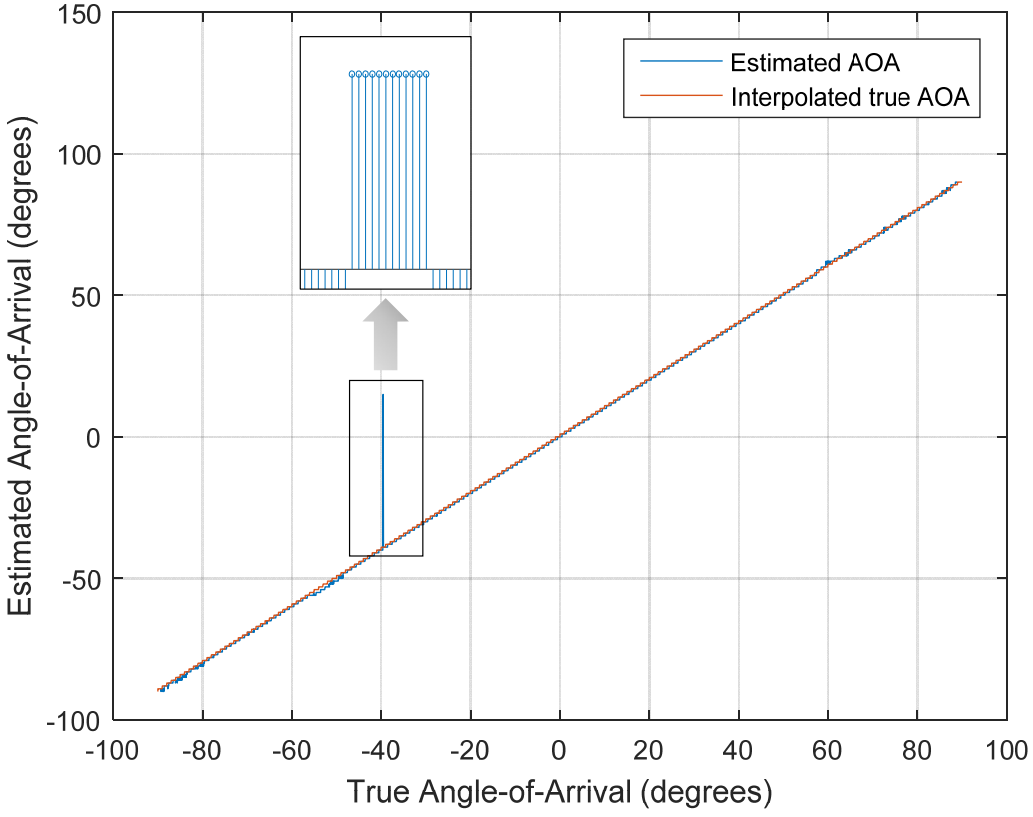

Figure 49. Outlier Data Extracted from P4 Signal (July 6, 2016)

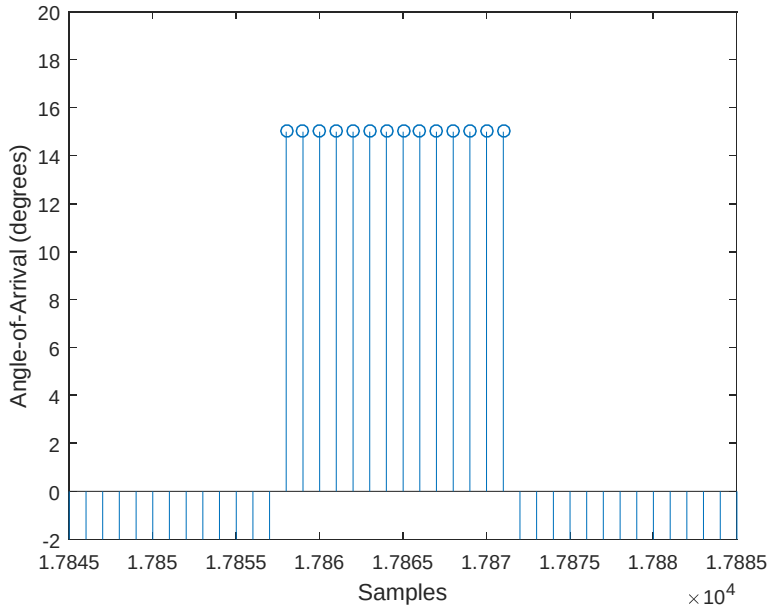

Figure 50. P4 Outlier Data #17856 to #17869 (July 6, 2016)

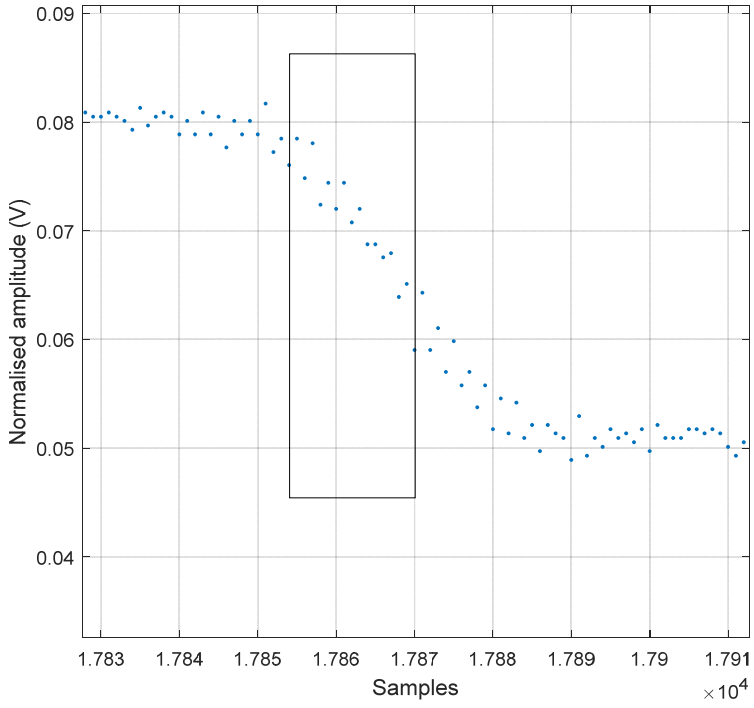

Figure 51. Raw Input Data that Correlates with the Outliers' Sample Numbers (P4 Signal)

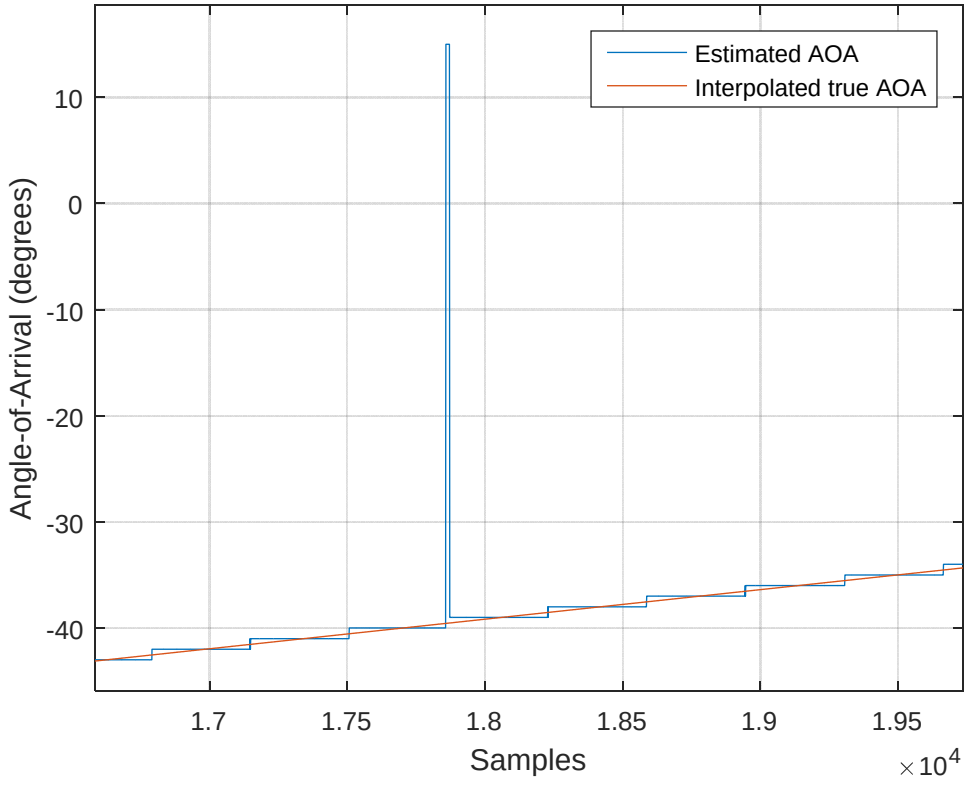

Figure 52. Zoom-in View Showing P4 Outliers

2. P4 Outlier Data Collected on July 13, 2016

The next set of outlier data analyzed were those collected on July 13, 2016 and shown in Figure 53. Similar to the analysis performed for P4 outliers collected on July 6, 2016, the minimum-Euclidean distance for outliers #2471 and #2481 were computed. The results are shown in Table 6. The analysis shows that #2471 was classified incorrectly as –61° and #2481 was classified incorrectly as –62° when the correct AOA for both outliers should have been 21°.

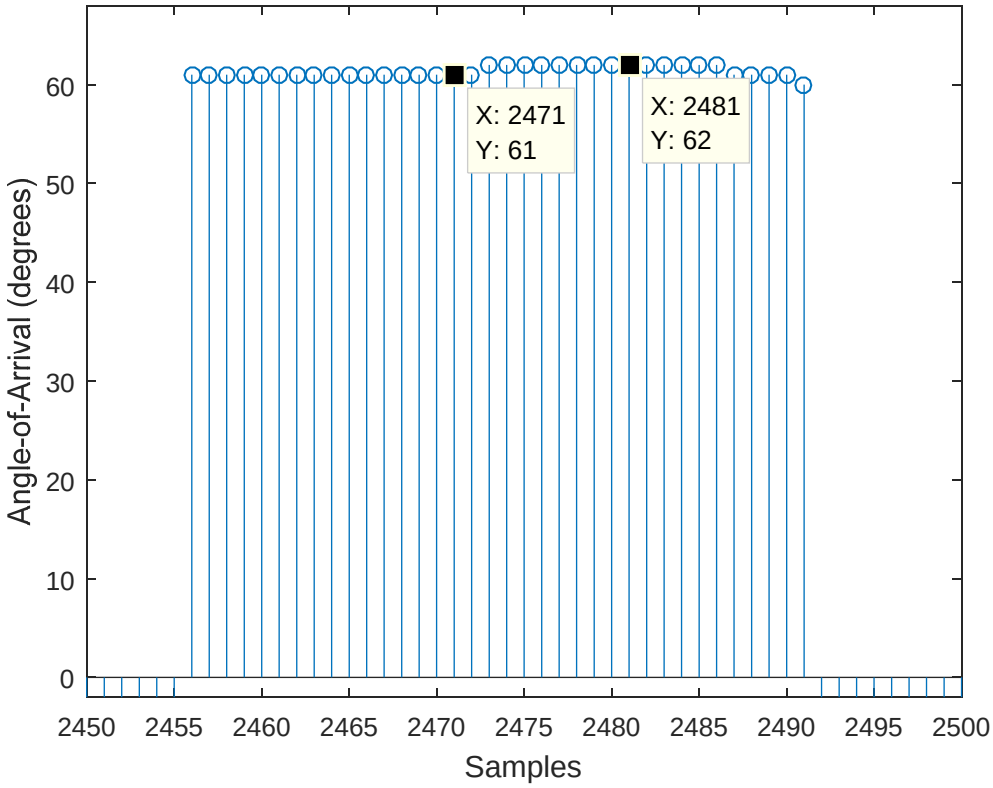

Figure 53. P4 Outlier Data #2456 to #2491 (July 13, 2016)

Table 6. Minimum-Euclidean Distance Calculations for Outliers #2471 and #2481

Angle (degrees)	Minimum-Euclidean distance	
	#2471	#2481
–21	0.00409	0.00365
61	0.0035	-
62	-	0.0034

3. FMCW Outlier Data Collected on July 6, 2016

FMCW outlier data #18193 through #18195 shown in Figure 54 were selected for analysis. From the minimum-Euclidean distance calculations shown in Table 7, we

observe that both the outliers were incorrectly classified with an AOA of 15° when their true AOA was –40°.

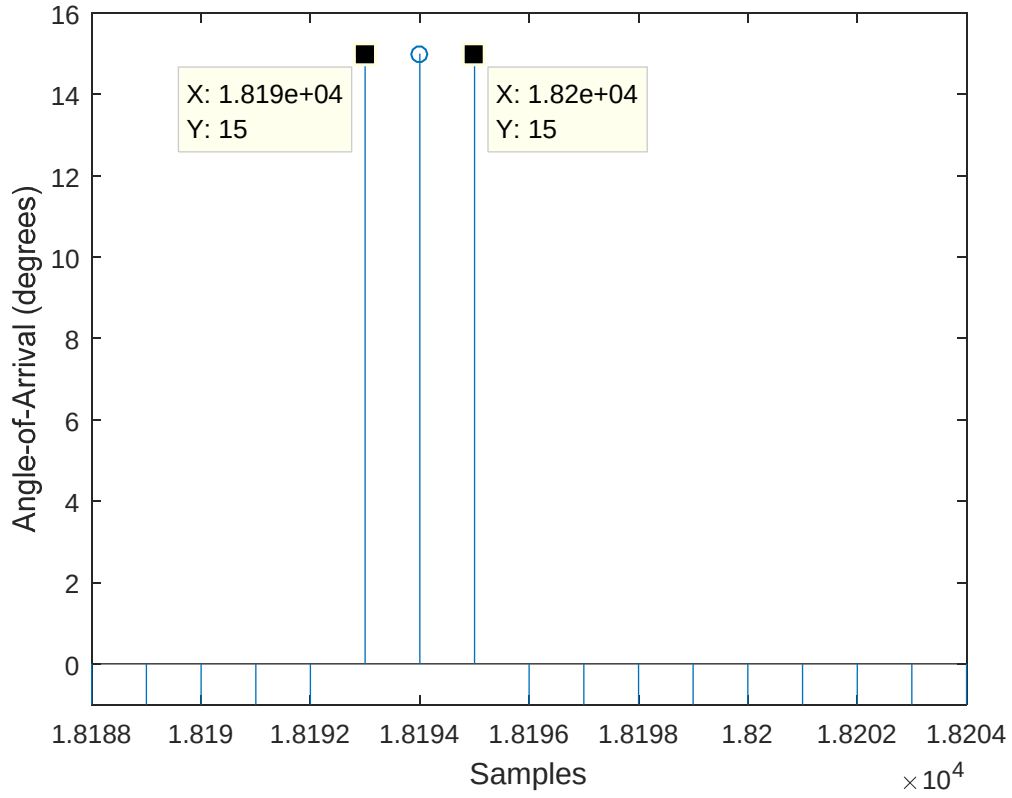

Figure 54. FMCW Outlier Data #18193 to #18195 (July 6, 2016)

Table 7. Minimum-Euclidean Distance Calculations for Outliers #18193 and #18195

Angle (degrees)	Minimum-Euclidean distance	
	#18193	#18195
–40	0.00091	0.00129
15	0.00084	0.00088

4. FMCW Outlier Data Collected on July 13, 2016

FMCW outlier data #3708 through #3774 shown in Figure 55 were selected for analysis. From the minimum-Euclidean distance calculations shown in Table 8, we observe that outliers #3708 and #3774 were both incorrectly classified with an AOA of –39° when their true AOAs were 14° and 15°, respectively.

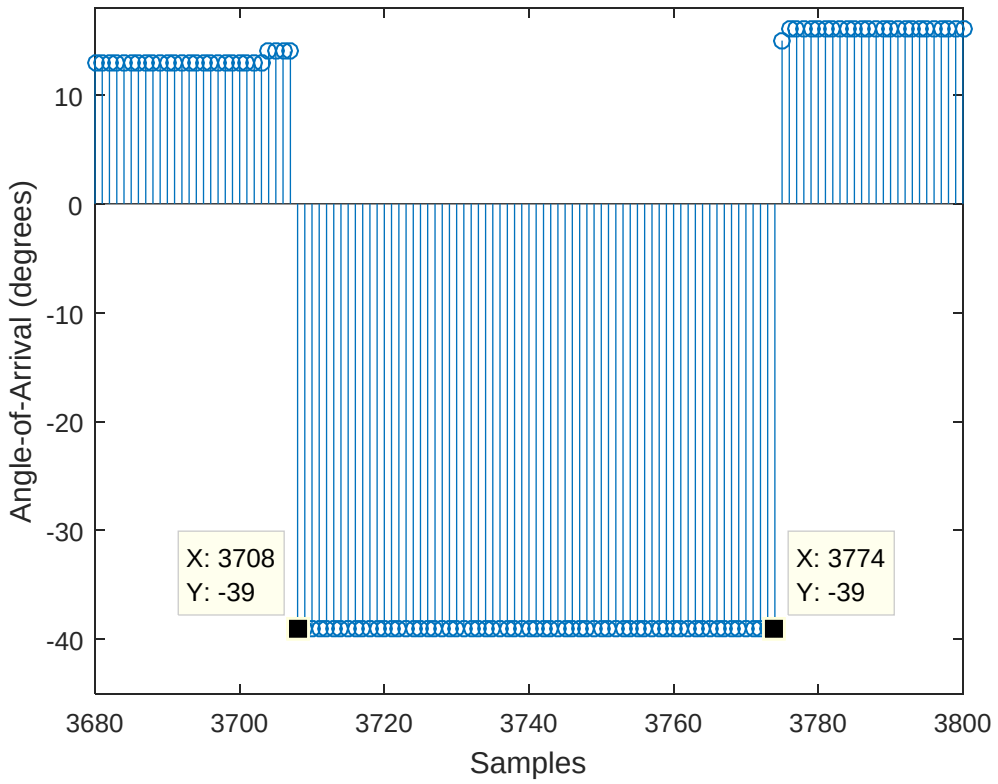

Figure 55. FMCW Outlier Data #3708 to #3774 (July 13, 2016)

Table 8. Minimum-Euclidean Distance Calculations for Outliers #3708 and #3774

Angle (degrees)	Minimum-Euclidean distance	
	#3708	#3774
–39	0.00153	0.00162
14	0.00169	-
15	-	0.00197

A critical conclusion to be drawn from the outlier analysis is that three MZM channels are insufficient to provide unique AOA estimation for resolution better than 1° or to cope with signals corrupted by noise. A recommended mitigation measure is the implementation of an additional MZM channel. This would result in AOA being determined by a vector consisting of four unique values instead of the current vector size of three [14]. This new approach would result in a marginal increase in system complexity but could be a worthwhile trade-off for reducing erroneous AOA estimation.

VI. CONCLUDING REMARKS AND FUTURE CONSIDERATIONS

Simulation of the MZM in MATLAB showed that the MZM modeling for saw-tooth and sine wave inputs were comparable to the measurements performed on the actual hardware. The MZM model was subsequently incorporated into the full system design. Further simulation demonstrated that the system model is capable of detecting LPI signals and lends credibility to subsequent hardware design and system testing.

The experimental tests conducted show that the system is capable of detecting and estimating the AOA for P4 and FMCW signals over a field-of-view of 180°. For FMCW, it was demonstrated that the system is capable of estimating the AOA with an RMS error of 0.29° at 1° resolution. For a P4-coded signal, the RMS error for the AOA estimation was 0.32° at 1° resolution. Further investigation of the outlier data showed that the current system design produces erroneous AOA estimations for angle resolution below 1°, and for data corrupted by noise. To minimize these errors, an additional MZM channel can be added with the trade-off of a marginally more complex system design. This is a potential area for future research.

The use of a minimum-Euclidean distance detector for AOA estimation proved to be a feasible and robust approach. Compared to its predecessor, which used an MLP neural network, the current AOA estimation technique does not require training data nor does it need frequent system calibration and retraining. Experimental results show that even with a one-week period between two successive tests, no significant deterioration of the AOA estimation accuracy was observed. In fact, the system was able to maintain the RMS error within 1° with only one calibration performed on the first run. This technique was proven to produce accurate and consistent results with minimal operator intervention.

Improvement to the software architecture allows for deterministic sampling up to 100-kHz. The current maximum sampling rate is limited to 10 kHz due to the lack of high-speed data streaming hardware. With suitable data streaming devices, the system can be further enhanced to perform AOA estimation for pulse-like signals.

Finally, it would be worthwhile to consider the identification of LPI signals using microwave-photonics. A preliminary experimental test was conducted to investigate the feasibility of this approach. The test setup is shown in Figure 56. The same P4-coded signal used in the anechoic chamber system test were fed to one end of the MZM electrode, while the other electrode was fed with the carrier frequency of the P4 signal from a coherent source. The envelope of the output of the MZM is captured by the RTO2044 oscilloscope as shown in Figure 57. We observed that the P4 signal has a sub-code period of 0.5 μs, which is consistent with the P4 signal used for the experimental test. Furthermore, if the carrier signal is coherent with the P4 signal, the envelope of the MZM output will be repeatable. This characteristic can be exploited for the identification of the modulation used in LPI signals.

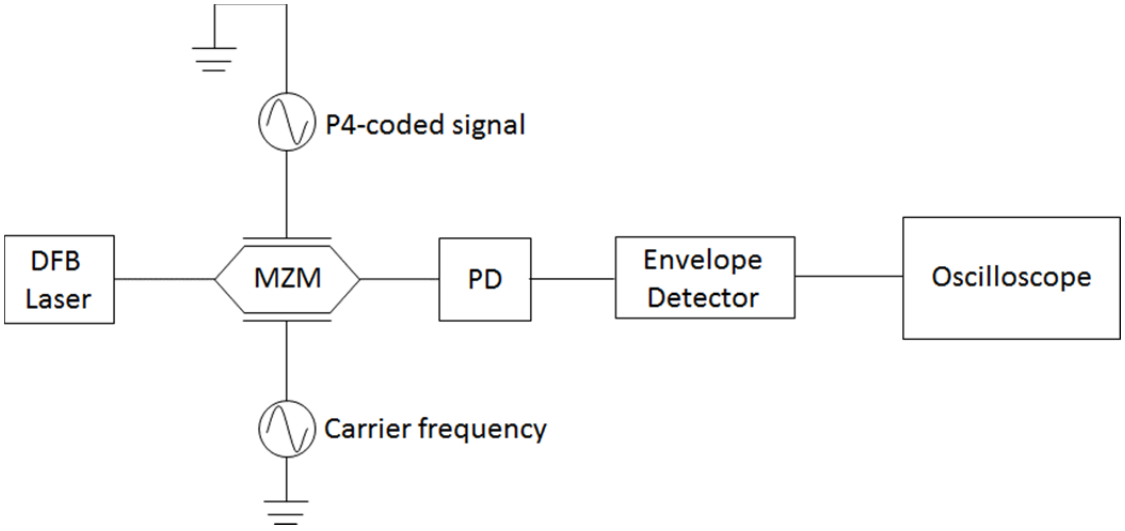

Figure 56. Test Setup for P4 Signal Identification

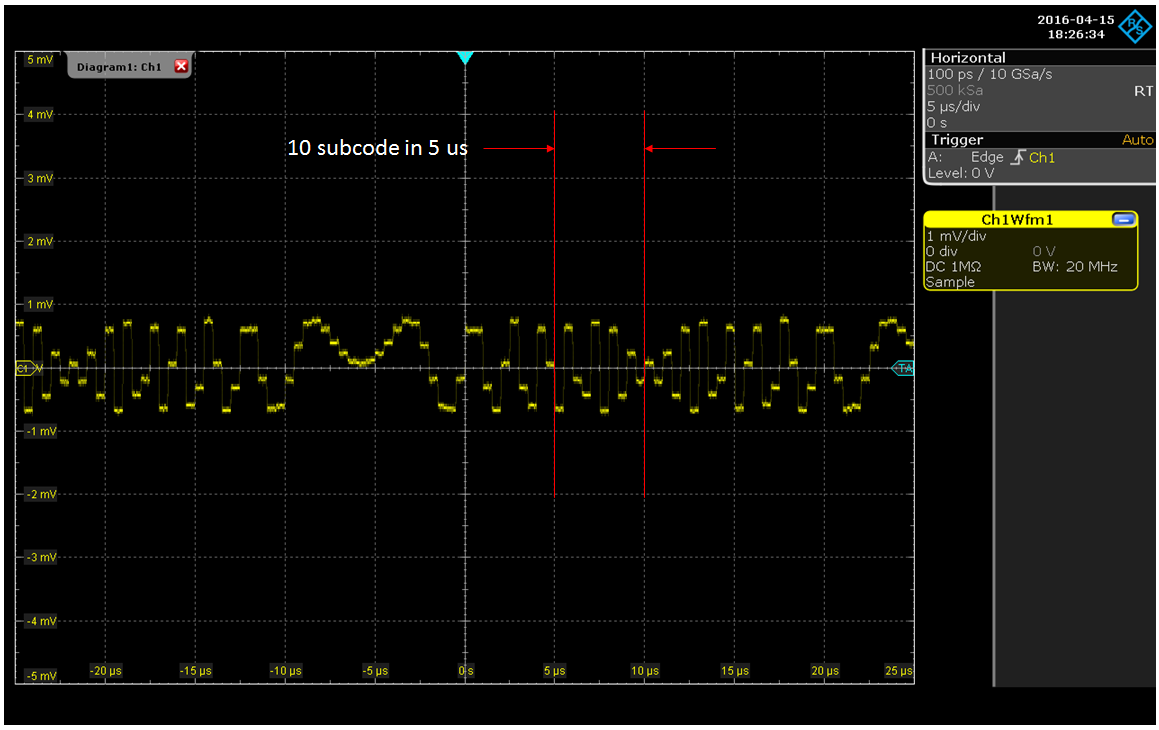

Figure 57. Envelope of Output of MZM for P4 signal

THIS PAGE IS INTENTIONALLY LEFT BLANK

APPENDIX. MATLAB CODE FOR SYSTEM SIMULATION

Matlab code for MZM simulation

```
% Created by: Ong Chee Kiong
% Created on: 2/21/2016
%

close all;
angle_of_arrival_degrees = 90; %angle of arrival in degrees
angle_of_arrival = angle_of_arrival_degrees/180*pi;

A = 1; %carrier amplitude
f_carrier = 1e3; %carrier frequency in Hz
wavelength = 3e8/f_carrier; %carrier wavelength in meters
antenna_separation = 0; %antenna separation in units of wavelength
modulator_arms_mismatch = 0; %assuming arms mismatch of zero for Mach
Zehnder Modulator
V_pi = 4; %V_pi of modulator
V_bias = 2; %bias voltage

phase_angle = computePhaseAngle(antenna_separation, ...
wavelength,angle_of_arrival);

phase_bias = computePhaseBias(modulator_arms_mismatch, ...
wavelength,V_bias,V_pi);
%t = linspace(0,0.1,300);
V1 = [I(16:7680)' I(1:15)']';
V2 = I;

V_diff = computeVoltageDiff(V1,V2);

T_factor = computeTransmissionFactor(V_diff,V_pi,phase_bias);

figure(1);
subplot(311);
plot(T_factor,'LineWidth',1);
title('MZM Output');
hold on
grid on
xlabel('Samples')
ylabel('Amplitude (Volts)')
subplot(312);
plot(V1,'LineStyle','-','LineWidth',1);
title('Input signal V1');
grid on;
xlabel('Samples')
ylabel('Amplitude (Volts)')
subplot(313);
plot(V2,'LineStyle','-','LineWidth',1);
grid on;
%legend('Modulator Output','Signal 1','Signal 2')
```

```
xlabel('Samples')
ylabel('Amplitude (Volts)')
title('Input signal V2');
%ylim([-1.2*amplitude 1.7*V_pi])

function [ phase_angle ] = computePhaseAngle( ...
antenna_separation, ...
wavelength, ...
angle_of_arrival)
%COMPUTEPHASEANGLE Summary of this function goes here
% Detailed explanation goes here
phase_angle = 2*pi*antenna_separation*sin(angle_of_arrival)/wavelength;
end

function [ phase_bias ] = computePhaseBias( ...
modulator_arms_mismatch, wavelength, V_bias, V_pi)
%COMPUTEPHASEBIAS Summary of this function goes here
% Detailed explanation goes here
phase_bias = 2*pi*modulator_arms_mismatch/wavelength + ...
pi*V_bias/V_pi;
end

function [ T_factor ] = computeTransmissionFactor( ...
V_diff, V_pi, phase_bias)
%COMPUTETRANSMISSIONFACTOR Summary of this function goes here
% Detailed explanation goes here
T_factor = 0.5*(1+cos(V_diff*pi/V_pi/2 + phase_bias));
% T_factor = cos(pi*V_diff/V_pi/2).^2;
end

function [ V_diff ] = computeVoltageDiff( ...
V1, V2)
%COMPUTEVOLTAGEDIFF Summary of this function goes here
% Detailed explanation goes here
V_diff = V1-V2;
end
```

Matlab code for system simulation

```
% Created by: Ong Chee Kiong
% Created on: 2/21/2016
%
% define sweep angles
AOA_deg = -90:1:90; %angle of arrival in degrees
AOA_rad = AOA_deg*pi/180; %angle of arrival in radians

% signal of interest parameters
A = 0.5; %carrier amplitude
fc = 1e3; %carrier frequency in Hz
fs = 50*fc; %set sampling rate to be 50 times of fc
wavelength = physconst('LightSpeed')/fc; %carrier wavelength in meters

% antenna separation between ref and ant1
antenna_separation_1 = 1.4*wavelength;
```

```
% antenna separation between ref and ant2
antenna_separation_2 = 1.6*wavelength;

% antenna separation between ref and ant3
antenna_separation_3 = 1.828*wavelength;

% MZM parameters
modulator_arms_mismatch = 0;
V_pi = 4;
V_bias = 0;

% define time vector for signal to be 3 cycle of fc
t = 0:1/fs:20/fc;

% define input reference V1
% uncomment for FMCW signal
fm = 1000;
tm = 0.05;
t = 0:1/fs:tm;
V1_up = A*sin(2*pi*(fc-fm/2).*t + 2*pi*fm/(2*tm)*t.^2);
V1_down = A*sin(2*pi*(fc+fm/2).*t-2*pi*fm/(2*tm)*t.^2);
V1 = [V1_up V1_down V1_up V1_down V1_up V1_down];
VI = V1;
VQ = ones(1,length(VI));

% uncomment for CW signal
%V1 = A*sin(2*pi*fc*t);

% define channel output
channel1 = NaN;
channel2 = NaN;
channel3 = NaN;
AOA_axis = NaN;
phase_diff = NaN;
%figure(1)
%hold on

% sweep AOA for MZM1
phase_bias = computePhaseBias(modulator_arms_mismatch, ...
wavelength,V_bias,V_pi);
for i=1:length(AOA_rad)
phase_diff_1 = computePhaseAngle(antenna_separation_1, ...
wavelength,AOA_rad(i));
% uncomment for FMCW signal
V12 = V1*exp(j*(phase_diff_1 + 0.8*pi));
V12 = real(V12);
% uncomment for CW signal
%V12 = A*sin(2*pi*fc*t + phase_diff_1 + 0.8*pi);
T1 = computeTransmissionFactor(V1-V12,V_pi,phase_bias);
% plot(T1);
T1 = T1-mean(T1);
[u, l] = envelope(T1,10,'peak');
channel1 = [channel1 -l(20:29)];
```

```
phase_diff_2 = computePhaseAngle(antenna_separation_2, ...
wavelength,AOA_rad(i));
V12 = V1*exp(j*(phase_diff_2 + 1.2*pi));
V12 = real(V12);
%V12 = A*sin(2*pi*fc*t + phase_diff_2 + 1.2*pi);
T2 = computeTransmissionFactor(V1-V12,V_pi,phase_bias);
T2 = T2-mean(T2);
[u, l] = envelope(T2,10,'peak');
channel2 = [channel2 -l(20:29)];
phase_diff = [phase_diff phase_diff_2];

phase_diff_3 = computePhaseAngle(antenna_separation_3, ...
wavelength,AOA_rad(i));
V12 = V1*exp(j*(phase_diff_3 + 1.65*pi));
V12 = real(V12);
%V12 = A*sin(2*pi*fc*t + phase_diff_3 + 1.65*pi);
T3 = computeTransmissionFactor(V1-V12,V_pi,phase_bias);
T3 = T3-mean(T3);
[u, l] = envelope(T3,10,'peak');
channel3 = [channel3 -l(20:29)];

if i == 1
AOA_axis = [AOA_axis linspace(-90,AOA_deg(i),10)];
else
AOA_axis = [AOA_axis linspace(AOA_deg(i-1),AOA_deg(i),10)];
end
end

plot(AOA_axis,channel1/max(channel1))
hold on
plot(AOA_axis,channel2/max(channel2))
plot(AOA_axis,channel3/max(channel3))
legend('channel 1','channel 2','channel 3')
axis([-90 90 0 1.5]);
```

LIST OF REFERENCES

[1] P. E. Pace, *Detecting and Classifying Low Probability of Intercept Radar*. Norwood, MA, Artech House, 2009, pp. 1–63.

[2] D. C. Schleher, "LPI radar: Fact or fiction," *IEEE Aerosp. Electron. Syst.*, vol. 21, pp. 3–6, 2006.

[3] D. L. Adamy, *EW 101*. Boston, London, Artech House, 2000, pp. 143–174.

[4] R. W. Watt and J. F. Herd, "An instantaneous direct-reading radiogoniometer," *Jour. Inst. Electrical Engineers,* vol. 64, pp. 611–617, 1926.

[5] L. Lading, "Differential Doppler heterodyning technique," *Appl. Opt.,* vol. 10, pp. 1943–1949, 1971.

[6] A. R. Cusdin, A. F. Dadds and P. Mallinson, "Radio direction-finding using time of arrival measurements," U.S. Patent No. 4,797,679. Jan. 10 1989.

[7] A. G. Stove, "Linear FMCW radar techniques," in *IEEE Proceedings F-Radar and Signal Processing*, pp. 343–350, 1992.

[8] W. D. Wirth, "Polyphase coded CW radar," in *Spread Spectrum Techniques and Applications Proceedings, IEEE 4th International Symposium*, vol. 1, pp. 186–190, 1996.

[9] J. E. Fielding, "Polytime coding as a means of pulse compression," *IEEE Trans. Aerospace Electron. Syst.*, vol. 35, pp. 716–721, 1999.

[10] M. Burgos-Garcia, J. Sanmartin-Jara, F. Perez-Martinez, and J. A. Retamosa, "Radar sensor using low probability of interception SS-FH signals," *IEEE Aerosp. Electron. Syst.*, vol. 15, pp. 23–28, 2000.

[11] S. E. Craig, W. Fishbein, and O. E. Rittenbach, "Continuous-wave radar with high range resolution and unambiguous velocity determination," *IRE Transactions on Military Electronics*, vol. 1051, pp. 153–161, 1962.

[12] B. M. Horton, "Noise-modulated distance measuring systems," in *Proceedings of the IRE*, vol. 47, pp. 821–828, 1959.

[13] J. A. Smit and W. Kneefel, "RUDAR-an experimental noise radar system," *De Ingenieur*, vol. 83, pp. 99–110, 1971.

[14] R. Humeur, "A new high-resolution direction finding architecture using photonics and neural network signal processing for miniature air vehicle applications," M.S. thesis, ECE, Naval Postgraduate School, Monterey, CA, 2015.

[15] T. W. Tedesso, J. Calusdian, C. Sewing, and P. E. Pace. "Wideband direction finding using a photonic robust symmetrical number system technique," *Optical Engineering 53(11)*, p. 114109, 2014.

[16] C. K. Tan, "Microwave-photonic architecture for direction finding of LPI emitters: front-end analog circuit design and component characterization," M.S Thesis, ECE, Naval Postgraduate School, Monterey, CA, 2016.

[17] P. E. Pace, D. Wickersham, D. C. Jenn, S. Nathan. "High-resolution phase sampled interferometry using symmetrical number systems," *IEEE Transactions on Antennas and Propagation*, vol. 49, pp. 1411–1423, 2001.

[18] L. Zehnder. "A new interference refractor," *Journal for Instrument Tuition*, pp. 276–285, 1891.

[19] L. Mach. "On an interference refractor," *Instrument Tuition 12*, pp. 89–93, 1892.

[20] A. Chen and E. Murphy, *Broadband Optical Modulators: Science, Technology, and Applications*. Boca Raton, FL, CRC Press, 2011.

[21] H. K. Zienkiewics. "Wave theory of Mach Zehnder interferometer," *Aeronautical Research and Council Reports and Memoranda*, 1959.

[22] I. P. Kaminow. (2014). Optical modulators. [Online]. Available: http://www.accessscience.com/content/472700.

[23] Dual drive 10Gb/s LN modulator (FTM7921ER) datasheet. Fujitsu Compound Semiconductor, Inc. [Online]. Available: http://www.chipfind.net/datasheet/fujitsu/ftm7921er.htm

[24] 40 GHz and 45 GHz photodetectors. Newport Corp. [Online]. Available: https://www.newport.com/f/40-ghz-and-45-ghz-photodetectors.

[25] New Focus, High speed detector user's guide. Newport Corp. [Online]. Available: https://www.newport.com/medias/sys_master/images/images/h68/hba/8797113122846/High-Speed-Detectors-and-Receivers-User-s-Manual.pdf.

[26] Low barrier Schottky diode detector. Keysight technologies. [Online]. Available: http://literature.cdn.keysight.com/litweb/pdf/5952-8299.pdf?id=1000030411:epsg:dow.

INITIAL DISTRIBUTION LIST

1. Defense Technical Information Center
   Ft. Belvoir, Virginia

2. Dudley Knox Library
   Naval Postgraduate School
   Monterey, California